Herzig, P.M., Humphris, S.E., Miller, D.J., and Zierenberg, R.A. (Eds.), 1998
Proceedings of the Ocean Drilling Program, Scientific Results, Vol. 158

4. GEOCHEMISTRY AND SULFUR-ISOTOPIC COMPOSITION OF THE TAG HYDROTHERMAL MOUND, MID-ATLANTIC RIDGE, 26°N[1]

Peter M. Herzig,[2] Sven Petersen,[2] and Mark D. Hannington[3]

ABSTRACT

Eighty-five bulk samples consisting of varying proportions of pyrite, silica, and anhydrite and 82 mineral separates (pyrite, chalcopyrite) from the TAG hydrothermal mound were analyzed using Neutron Activation Analyses (INAA), Inductively Coupled Plasma Emission Spectrometry (ICP-ES), Inductively Coupled Plasma Mass Spectrometry (ICP-MS), and sulfur-isotopic methods. The samples were collected from five different areas of the Trans-Atlantic Geotraverse (TAG) mound during Ocean Drilling Program Leg 158. The chemistry of the bulk samples is dominated by high Fe (average 30.6 wt%, n = 57) and S concentrations (average 42.0 wt%, n = 50), reflecting the high amount of pyrite in these rocks. High Ca (up to 11.5 wt%, n = 57) and SiO_2 values (up to 49.8 wt%, n = 50) indicate the presence of anhydrite-rich zones in the center of the mound, and pyrite-silica breccias, silicified wallrock breccias, and paragonitized basalt breccias deeper in the system. The Cu and Zn concentrations vary from <0.01 to 12.2 wt% Cu (average 2.4 wt%, n = 57) and from <0.01 to 4.1 wt% Zn (average 0.4 wt%, n = 57), with highest values commonly occurring in the uppermost 20 m of the mound. Most trace-element concentrations are relatively low compared to other mid-ocean ridge hydrothermal sites and average 0.5 ppm Au, 43 ppm As, 234 ppm Co, 2 ppm Sb, 14 ppm Se (n = 85), 9 ppm Ag, 11 ppm Cd, and 59 ppm Pb (n = 57). Gold, Ag, Cd, Pb, and Sb behave similarly to Cu and Zn and are enriched close to the surface of the mound. This is interpreted as evidence for zone refining, a process in which elements that are mobilized from previously deposited sulfides in the interior of the mound by later hydrothermal fluids are transported to the surface, where they reprecipitate as a result of mixing with ambient seawater. The trace-element composition of pyrite and chalcopyrite separates is similar to the bulk geochemistry. However, down to about 50 mbsf, Au, As, Sb, and Mo values in pyrite separates are generally higher than in bulk samples and chalcopyrite separates. Below this depth, these elements appear to be enriched in chalcopyrite separates. Cobalt is typically more enriched in pyrite than in chalcopyrite throughout. A major difference between pyrite and chalcopyrite separates is the strong enrichment of Se in chalcopyrite at the top of the mound, whereas pyrite separates show a moderate increase of Se with depth. Sulfur-isotopic values for bulk sulfides from the interior of the TAG mound vary from +4.6‰ to +8.2‰, with an average of +6.4 ‰ $\delta^{34}S$ (n = 49). These values do not change significantly downhole, but samples collected from the top of the mound appear to have somewhat lower $\delta^{34}S$ values than samples from the interior. The average $\delta^{34}S$ value for TAG sulfides is about 3‰ higher than for most other sulfides generated at sediment-free mid-ocean ridges (average 3.2‰, n = 501). This is largely attributed to thermochemical sulfate (anhydrite) reduction by high-temperature hydrothermal fluids upwelling through the interior of the TAG mound.

INTRODUCTION

In September-November 1994, Ocean Drilling Program Leg 158 intersected for the first time an active hydrothermal system on a sediment-free mid-ocean ridge. Drilling target was the active Trans-Atlantic Geotraverse (TAG) hydrothermal mound located at a water depth of 3650 m in the TAG hydrothermal field at the Mid-Atlantic Ridge, 26°N. Seventeen holes drilled at five locations on the TAG mound reveal the subsurface nature and lateral heterogeneity of this actively forming deposit and establish the extent of the underlying alteration zone down to a depth of 125 mbsf (Humphris et al., 1995). This paper describes the major- and trace-element geochemistry and the sulfur-isotopic composition of samples recovered from the interior of the TAG hydrothermal mound.

GEOLOGIC SETTING

The TAG hydrothermal field extends over an area of at least 5 × 5 km and is located at the base and slope of the eastern wall of the Mid-Atlantic Ridge at 26°N (Fig. 1). It consists of presently active low- and high-temperature zones, as well as a number of relict deposits that in part may be related to small volcanic centers (Rona et al., 1996). The zone of low-temperature hydrothermal activity occurs between 2400 and 3100 m depth on the eastern wall of the rift valley and includes massive, layered deposits of Mn oxide, amorphous Fe oxide, and nontronite (Rona et al., 1984; Thompson et al., 1988). Two large relict zones are located on the lower east wall. The *Alvin* zone consists of several discontinuous sulfide deposits associated with mound-like features with dimensions similar to the active mound. The *Mir* zone is a large sulfide deposit displaying various stages of seafloor weathering and locally has numerous inactive standing and toppled sulfide chimneys up to 25 m in height (Rona et al., 1993).

The active TAG hydrothermal mound (Fig. 1) is a distinctly circular feature, about 200 m in diameter and 50 m in height, located at a water depth of 3650 m on oceanic crust at least 100 ka (Rona et al., 1986). The mound exhibits two distinct, flat platforms that may represent two phases of active growth (Kleinrock et al., 1996). Radiometric dating of sulfides has been interpreted to indicate that the formation of massive sulfides at the TAG mound started about 50–20 ka, with high-temperature pulses every 5000–6000 years (Lalou et al., 1993). The present high-temperature activity apparently commenced about 60 yr ago.

Numerous submersible studies have described that the dominating hydrothermal feature of the active TAG mound is the Black Smoker Complex which is located on a 10- to 15-m high, 20- to 30-m diameter cone located northwest of the center. This complex consists of an unknown number of highly active black smoker chimneys (chalcopyrite-anhydrite-pyrite) venting fluids at temperatures of up to 363°C (Edmond et al., 1995). A group of white smokers (domi-

[1]Herzig, P.M., Humphris, S.E., Miller, D.J., and Zierenberg, R.A. (Eds.), 1998. *Proc. ODP, Sci. Results*, 158: College Station, TX (Ocean Drilling Program).

[2]Lehrstuhl für Lagerstättenlehre, Institut für Mineralogie, Technische Universität Bergakademie Freiberg, Brennhausgasse 14, D-09599 Freiberg, Federal Republic of Germany. Herzig: herzig@mineral.tu-freiberg.de

[3]Geological Survey of Canada, 601 Booth Street, Ottawa, Ontario K1A 0E8, Canada.

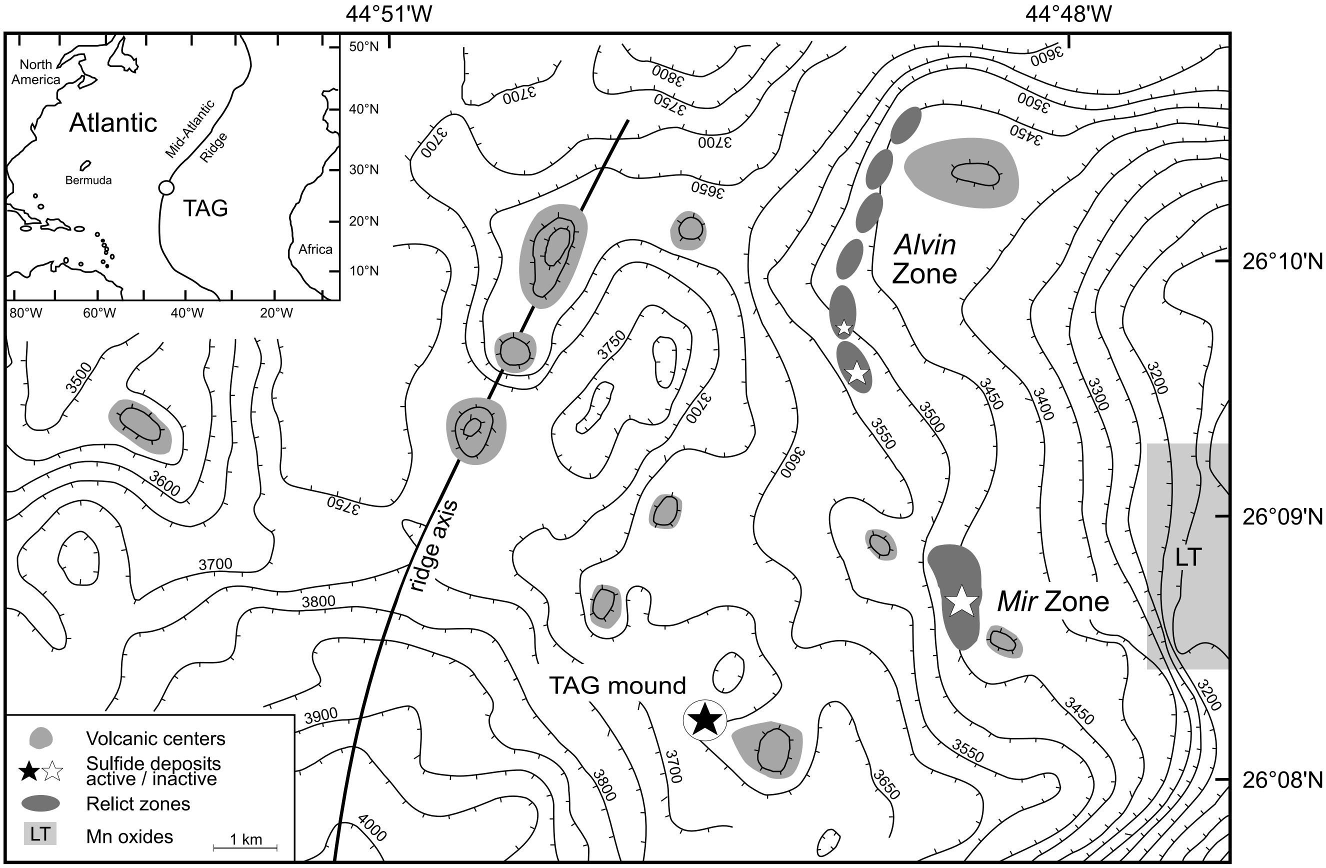

Figure 1. SeaBeam bathymetry (50-m contour interval) of the TAG hydrothermal field showing the locations of volcanic domes, the active TAG mound, the low-temperature hydrothermal field (LT) up on the eastern rift valley wall, and the *Alvin* and *Mir* relict hydrothermal zones (after Rona et al., 1993).

nantly sphalerite-pyrite), venting fluids at 260°–300°C, is located approximately 70 m southeast of the Black Smoker Complex (Kremlin area). Mass wasting of the edges of the inner mound results in steep outer slopes covered with pyrite-rich blocks containing trace amounts of amorphous silica, quartz, and goethite, and outer oxidized layers that include atacamite, amorphous Fe oxides, goethite, hematite, amorphous silica, and locally high concentrations of gold (Herzig et al., 1991). The outer mound is surrounded by an apron of carbonate and metalliferous sulfide-oxide sediment that extends up to about 100 m away from the mound.

SUMMARY OF DRILLING RESULTS

Seventeen holes drilled at five locations on the active TAG mound (TAG-1 to 5; Fig. 2) revealed the overall internal structure of the mound and the underlying upflow zone down to a maximum depth of 125 mbsf (TAG-1 area). Based on composite sections for each area (Fig. 2), four major lithologic zones can be distinguished (Humphris et al., 1995; Fig. 3): Zone 1 (0–20 mbsf) consists of massive pyrite and massive pyrite breccias with pyrite clasts up to 5 cm in a matrix of porous, sandy pyrite and is locally overlain by Fe oxyhydroxides and cherts. Zone 2 (20–45 mbsf) contains pyrite-anhydrite breccias with rounded pyrite clasts (up to 2 cm) cemented by anhydrite down to 30 mbsf. This is followed by pyrite-silica-anhydrite breccias, which are made up of clasts of siliceous pyrite, quartz-pyrite aggregates, and granular pyrite in a quartz matrix. The pyrite-silica-anhydrite breccias are commonly crosscut by anhydrite veins up to 45 cm in thickness. Zone 3 (45–100 mbsf) is dominated by pyrite-silica breccias (gray fragments of preexisting mineralized and silicified wallrock and quartz-pyrite clasts in a matrix of fine-grained quartz) grading into silicified wallrock breccias that consist of clasts of basaltic fragments (up to 5 cm) that are recrystallized to quartz, pyrite, and smectite. This zone is interpreted to comprise the upper part of the stockwork zone. Zone 4 (100–125 mbsf) is dominated by altered basalt breccias composed of chloritized and paragonitized, weakly mineralized basalt fragments (up to 5 cm) in a matrix of quartz and pyrite, crosscut by veins of pyrite, quartz, and quartz + pyrite. This zone is thought to represent the lower part of the stockwork and upflow zone beneath the TAG mound.

SAMPLES AND METHODS

A total of 85 bulk samples consisting of varying proportions of pyrite, silica, and anhydrite from areas TAG-1 to 5, and 82 handpicked pyrite and chalcopyrite separates from the TAG-1 area were selected for Neutron Activation Analyses (INAA), Inductively Coupled Plasma Emission Spectrometry (ICP-ES) and Inductively Coupled Plasma Mass Spectrometry (ICP-MS) using standard analytical procedures; sulfur was analyzed with a Leco system. Sulfur-isotopic analyses were conducted on bulk sulfide samples following the method of Ueda and Krouse (1986). Prior to analysis, anhydrite was removed from the samples by dissolution of $CaSO_4$ using artificial seawater. Following this process, selected samples were analyzed by Atomic Absorption Spectrophotometry (AAS) to prove complete Ca (and thus anhydrite) removal. Sulfur isotope ratios are reported in standard delta notation relative to the Canyon Diablo Troilite (CDT). Replicate analysis of standards yields a standard deviation of less than 0.2%. Sulfur dioxide gas for mass spectrometric analysis was prepared by combustion of sulfides with V_2O_5 and quartz at 950°C and analyzed for sulfur-isotopic ratios using a Finnigan Delta E mass

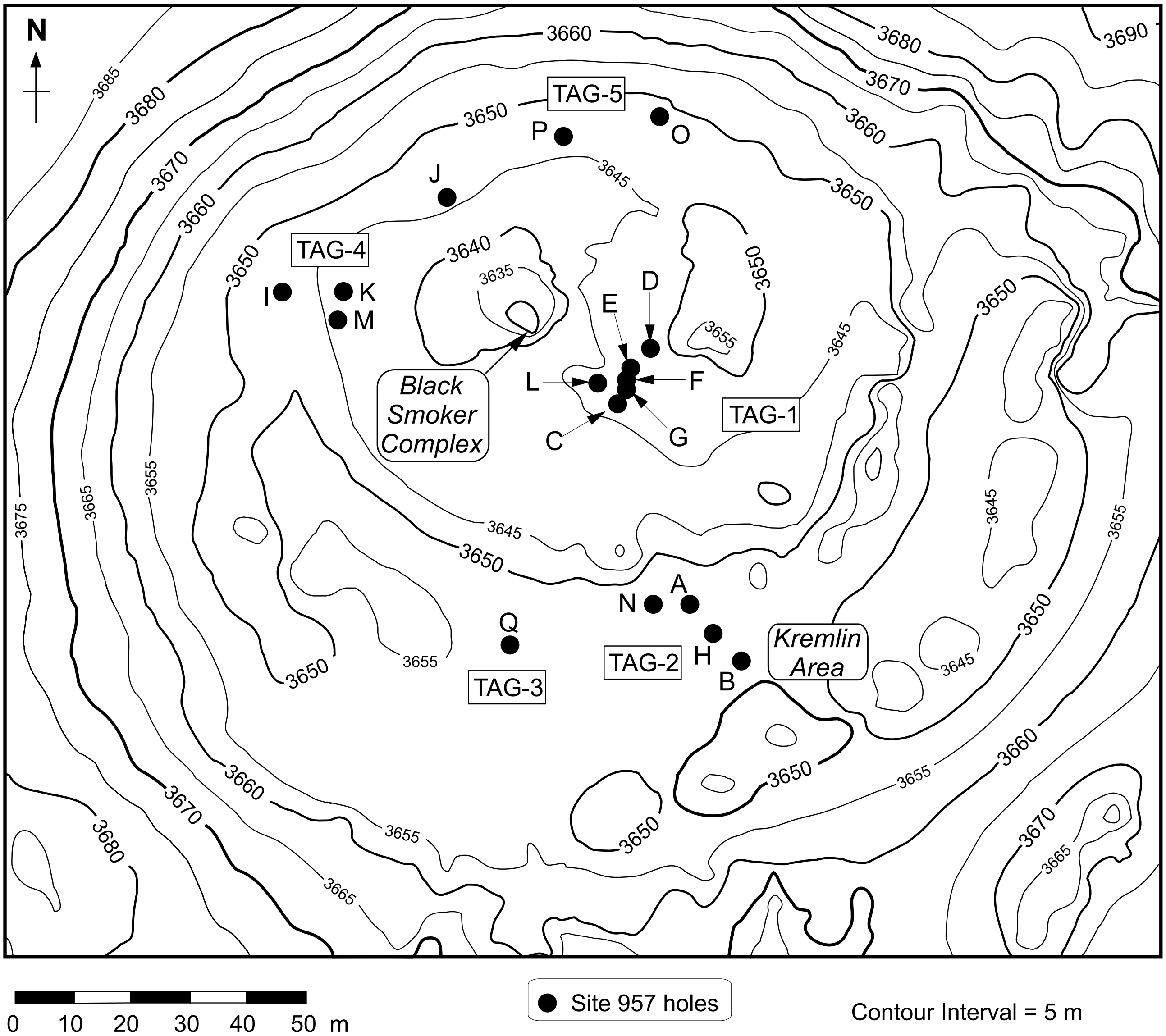

Figure 2. High-resolution bathymetric map (5-m contour interval) of the active TAG mound (Kleinrock et. al., 1996) showing the upper and lower platforms, the area of black smoker venting (Black Smoker Complex), and the area of white smoker venting (Kremlin area). The location of the holes drilled during Leg 158 in five different areas of the mound (TAG-1 to -5) are also shown.

spectrometer. Sample designation, depth interval, analytical method with detection limits, and the geochemical composition of the samples are given in the data report by Hannington et al. (Chap. 2, this volume) and in Brügmann et al. (Chap. 7, this volume). As indicated in Table 1, the emphasis of this study is the TAG-1 area (in which Hole 957E reached the maximum penetration of 125 mbsf) with 40 bulk samples, 56 pyrite, and 25 chalcopyrite separates analyzed. Selected bulk samples from the TAG-2 to TAG-5 areas were analyzed to document the lateral heterogeneity of sulfide mineralization.

RESULTS

Major- and Trace-Element Geochemistry

The major-element geochemistry of the bulk samples analyzed from holes drilled in the TAG-1 to 5 areas (Tables 1, 2) strongly reflects their mineralogical composition (Knott et al., Chap. 1, this volume). High Fe (3.8–48.1 wt%, average 30.6 wt%) and S (5–53.3 wt%, average 42 wt%) concentrations reflect the predominance of pyrite in the mound. Average Cu and, in particular, Zn concentrations are relatively low compared to other sediment-free mid-ocean ridge sulfides, reaching only 2.4 wt% Cu and 0.4 wt% Zn (Table 2). Locally, high amounts of Ca (up to 11.5 wt%) and SiO_2 (up to 49.8 wt%) occur in anhydrite-rich zones in the center of the mound and in silica-rich zones (pyrite-silica breccias, silicified wallrock breccias, and chloritized and paragonitized basalt breccias) deeper in the system. High SiO_2 concentrations also characterize chert fragments recovered from the surface of the mound (up to 92.7 wt%).

With the exception of Mo, most trace-element concentrations of the TAG bulk samples are relatively low when compared to samples from other sediment-free mid-ocean ridge sites and average 43 ppm As, 14 ppm Se, 11 ppm Cd, <10 ppm Ni, 3.5 ppm Tl, and 234 ppm Co (Table 2). In particular, the average concentrations of Ba (95 ppm), Pb (59 ppm), Ga (8 ppm), In (1 ppm), Sb (2 ppm), and Ag (9 ppm) are much lower than the average values for sulfides from sediment-free mid-ocean ridges (Table 2). Gold concentrations range from < 5 ppb to 3.2 ppm, with an average of only 0.5 ppm Au (n = 85), which is approximately half the average Au content of sulfides from sediment-free mid-ocean ridge sites (0.9 ppm Au, n = 829; Table 2).

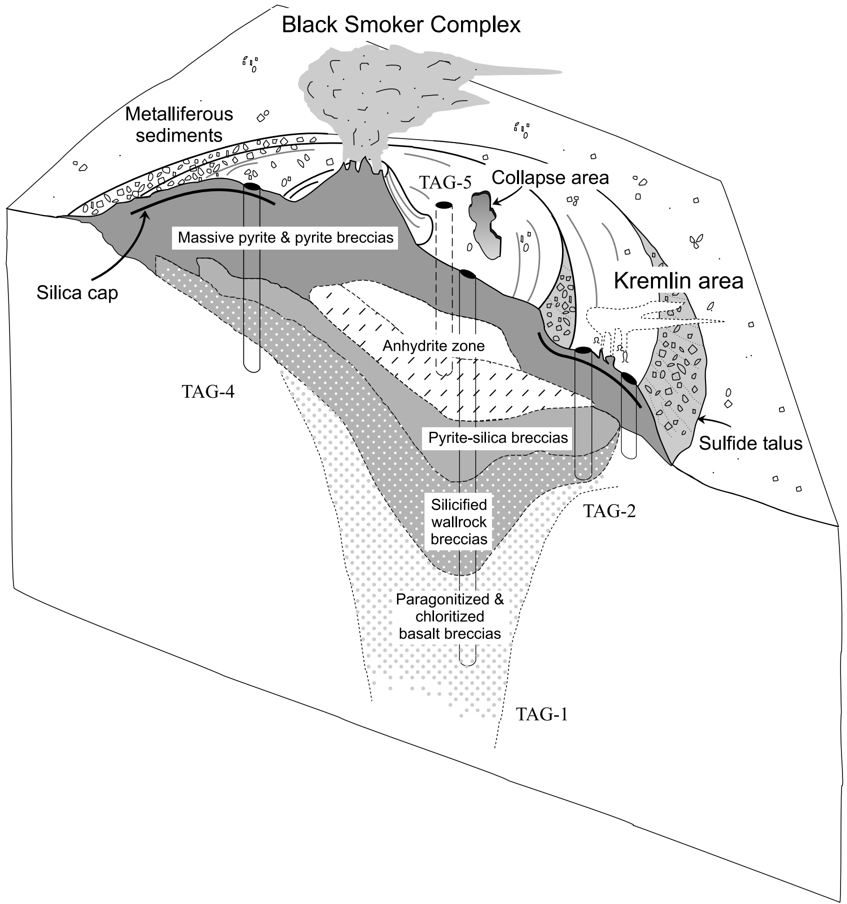

Figure 3. Schematic diagram of the TAG hydrothermal mound showing the surface morphology and distribution of venting, as well as the generalized and simplified internal structure based on the results of drilling during Leg 158.

Table 1. Number and types of samples analyzed from Leg 158 drilling areas TAG-1 to -5.

	Bulk samples	Pyrite separates	Chalcopyrite separates
TAG-1 (C, E, F, G)	40	56	25
TAG-2 (A, B, H, N)	12	1	
TAG-3 (Q)	4		
TAG-4 (I, J, K, M)	17		
TAG-5 (O, P)	12		

Note: Holes drilled in each area are shown in parentheses.

Lateral Heterogeneity of Major- and Trace-Element Compositions

A comparison of major- and trace-element data for the different drilling areas of the TAG mound indicates major differences that are related to variations in lithology (Table 3). The chemical composition of samples from the TAG-1 and TAG-5 areas is relatively similar, reflecting the similarities in the lithologies recovered, including a zone characterized by a relatively high abundance of anhydrite (3 and 2.6 wt% Ca, respectively). Cobalt and Se concentrations are higher than in the TAG-3 and TAG-4 areas, but similar to results obtained for samples from the TAG-2 area (Kremlin), whereas the concentrations of Zn and associated elements (Cd, Au, Ag, Sb, Pb, In, Ga) in the TAG-1 and TAG-5 areas are distinctly lower than in the TAG-2, -3, and -4 areas (Table 3).

Samples from the TAG-2 area (Kremlin) are characterized by the highest average Cu, Ag, Pb, Ga, and In concentrations, and elevated Zn concentrations (0.7 ppm). Relative to the other areas, samples from the TAG-4 area have the highest Zn, As, Cd, Mo, Sb, and Tl concentrations, high Pb, and the lowest Cu and Se concentrations.

Chemical Composition of Lithologic Units

In accordance with the initial shipboard core descriptions, the analyzed samples were grouped into six major lithologies including (1) Fe oxides and cherts recovered from the surface of the mound, (2) massive pyrite and massive pyrite breccia present in the uppermost part of the mound, (3) pyrite-anhydrite-silica breccia located in the central mound, (4) pyrite-silica breccia representing the upper stockwork zone, (5) silicified wallrock breccia, and (6) chloritized and paragonitized basalt breccia from the deeper stockwork zone (Table 4). The Fe oxides and cherts from the uppermost surface of the mound are characterized by relatively low average Fe concentrations (17.6 wt%) compared to the pyrite-bearing assemblages (average up to 34.5 wt% Fe), but high SiO_2 concentrations (average 61.7 wt%) reflecting the abundance of cherts. Copper and Zn in the uppermost surface layer average only 0.7 wt% and 0.5 wt%, respectively. Gold (1.1 ppm), Ag (18 ppm), Cd (17 ppm), Pb (120 ppm), and Sb (4 ppm) in the Fe oxides and cherts have concentrations similar to those found in the massive pyrite and massive pyrite breccia samples (1.1 ppm Au, 24 ppm Ag, 37 ppm Cd, 135 ppm Pb, 4.2 ppm Sb) and, in both units, are generally higher than the average values for the other lithologies. The massive pyrite and massive pyrite breccia samples are significantly enriched in Cu (average 4.2 wt%) and Zn (average 1.3 wt%) relative to the other units. The Cu concentration in the pyrite-anhydrite-silica breccias averages 2.9 wt%, whereas Zn concentrations average only 600 ppm. This is accompanied by low values for most trace elements except As, Co, Mo, and Se. The pyrite-silica breccias are typically characterized by high average SiO_2 concentrations (26.5 wt%), low Cu (1.5 wt%), and Zn (1200 ppm), with trace-element concentrations similar to those of pyrite-anhydrite-silica breccias and silicified wallrock breccias. Samples of silicified wallrock breccia and one sample of chloritized and paragonitized basalt

Table 2. Major- and trace-element composition of bulk sulfide samples from the interior of the TAG hydrothermal mound.

	TAG				MOR	
	Method	n	Range	Average	Average	n
Major elements (wt%)						
Fe	ICP-ES	57	3.8-48.1	30.6	24.9	1171
S	Leco	50	5.0-53.3	42.0	34.0	958
Cu	ICP-ES	57	0.01-12.2	2.4	4.0	1102
Zn	ICP-ES	57	<0.01-4.1	0.4	10.4	1158
SiO_2	ICP-ES	57	0.3-92.7	19.2	9.9	1021
Ca	ICP-ES	57	0.04-11.5	2.0	2.6	940
Trace elements (ppm)						
Au	INAA	85	<0.005-3.2	0.5	0.9	829
Ag	ICP-MS	57	0.3-160	9	111	1063
As	INAA	85	8-140	43	265	835
Ba	ICP-ES	57	<30-560	95	15500	992
Cd	ICP-ES	57	<0.5-200	11	293	726
Co	INAA	85	<5-750	234	311	1106
Cr	INAA	85	<10-79	23	25	724
Ga	ICP-MS	57	0.4-95	8	47	218
In	ICP-MS	57	<0.05-15	1	8.4	87
Mo	INAA	85	6-20	89	89	809
Ni	ICP-ES	57	<10-35	<10	47	970
Pb	ICP-MS	57	4-430	59	1200	1077
Sb	INAA	85	0.1-16	2	42	828
Se	INAA	85	<5-86	14	97	729
Tl	ICP-MS	57	0.2-30	3.5	28	158

Notes: The average chemical composition of massive sulfides from hydrothermal sites at sediment-free mid-ocean ridges (MOR) is given for comparison (S. Petersen and Geological Survey of Canada, unpubl. data). n = number of analyses.

Table 3. Comparison of the chemical composition of bulk sulfides from TAG-1 to TAG-5 areas.

	TAG-1	TAG-2	TAG-3	TAG-4	TAG-5
	(n = 25)	(n = 5)	(n = 4)	(n = 13)	(n = 10)
ICP (wt%)					
Fe	31.6	27.8	15.1	33.0	32.5
S	42.1	38.3	41.2	39.9	45.7
Cu	2.0	4.6	2.5	1.1	3.7
Zn	<0.1	0.7	0.3	1.3	<0.1
SiO_2	14.4	24.2	62.3	22.0	7.7
Ca	3.0	1.6	0.1	<0.1	2.6
ICP (ppm)					
Ag	1	48	9	12	3
Ba	86	74	34	125	112
Cd	<1	19	15	35	2
Ga	2	22	12	16	4
In	0.3	4.3	2.1	1.0	1.0
Pb	21	154	59	115	34
Tl	1.8	2.5	1.2	8.8	2.5
	(n = 40)	(n = 12)	(n = 4)	(n = 17)	(n = 12)
INAA (ppm)					
Au	0.2	0.9	1.3	1.0	0.3
As	36	32	31	66	46
Co	254	250	42	113	385
Cr	22	28	11	20	30
Mo	85	70	31	115	104
Sb	0.7	3.0	2.3	4.2	1.0
Se	14	16	<5	<5	34

Note: n = number of analyses.

appear to have similar average major and trace element concentrations.

The Fe and S concentrations clearly indicate the abundance of pyrite in the upper part of the mound down to pyrite-silica breccias, averaging 31.7–34.5 wt% Fe and 40–46.4 wt% S. Low SiO_2 concentrations (except for the surface cherts) are typical for the upper part of the mound, whereas the beginning of the stockwork zone is marked by a strong increase in SiO_2. The average Cu concentration is highest in the massive pyrite and massive pyrite breccias (average 4.2 wt%), but also high in pyrite-anhydrite breccias because of the presence of chalcopyrite selvages on anhydrite veins and disseminated chalcopyrite in massive anhydrite. High concentrations of Cu are found in the massive pyrite and pyrite breccias, and pyrite-anhydrite ± silica breccias, whereas Zn is only concentrated in the massive pyrite and pyrite breccias (average 1.3 wt%). The Ca values clearly reflect the dominance of anhydrite in the pyrite-anhydrite-silica breccias (average 4.1 wt%). The relatively high Ca content of the silicified wallrock breccias (average 2.4 wt%) is largely the result of the local occurrence of anhydrite veins in these breccias. The variation of Au concentrations is similar to those observed for Cu, with highest concentrations in Fe-oxides/cherts (1.1 ppm) and the massive pyrite and pyrite breccias (1.1 ppm). The lowest concentrations were measured in the chloritized and paragonitized basalt sample (60 ppb) which, however, is still enriched in Au relative to the average Au content of mid-ocean ridge basalt (MORB; 1 ppb Au; Crocket, 1991). Most trace elements follow the same trend with the exception of Co and Se, which appear to be enriched in the lower parts of the mound.

Downhole Distribution of Major- and Trace-Elements in the TAG-1 to TAG-5 Areas

TAG-1 Area (Black Smoker Complex)

The downhole distribution of selected major elements in the TAG-1 area close to the Black Smoker Complex is given in Figure 4. The Fe and S concentrations are positively correlated and reflect the presence of pyrite-bearing breccias. Silica concentrations are highly variable, but consistently high below 50 mbsf (except for Sample 158-957E-12R-1, 16–20 cm, at 92 mbsf, which contains abundant vein-related pyrite). The Ca concentration is high in samples originating from the upper part of the mound and the pyrite-anhydrite zone, and decreases in the stockwork zone. Copper is enriched in the upper part of the TAG-1 area. Higher values in deeper parts of the mound correspond to the occurrence of disseminated chalcopyrite in anhydrite veins. Zinc concentrations are generally low, but relatively elevated in the upper 45 m. Gold, Ag, Sb, In, and Ga concentrations appear to decrease downhole. Cadmium typically mirrors the downhole distribution of Zn, consistent with its occurrence as a trace component in sphalerite. Lead and As concentrations are generally low, without any downhole variation. The vertical distribution of Co and Mo is erratic. The small increase in Se concentration at the surface of the mound is likely a result of the presence of collapsed chimney fragments, which have been shown to contain high Se contents (Tivey et al., 1995). Most element concentration vs. depth profiles exhibit large variability within the pyrite-anhydrite zone.

A comparison of the chemical composition of bulk samples with pyrite and chalcopyrite separates from the TAG-1 area indicates some contrasting trends (Fig. 5). Similar to the downhole Au distribution in bulk samples, the pyrite separates indicate an enrichment of

Table 4. Comparison of the chemical composition of different lithologic zones identified in drill cores from the TAG hydrothermal mound.

	Cherts/ Fe oxides	Massive pyrite + pyrite breccias	Pyrite-anhydrite ± silica breccias	Pyrite-silica breccias	Silicified wallrock breccias	Chloritized basalt breccias
	(n = 6)	(n = 12)	(n = 15)	(n = 15)	(n = 8)	(n = 1)
ICP (wt%)						
Fe	17.6	34.9	33.5	30.3	29.2	29.1
S	5.0	45.7	46.3	40.0	37.7	37.1
Cu	0.7	4.3	3.0	1.5	1.5	>0.1
Zn	0.52	1.44	0.05	0.12	0.01	0.01
SiO_2	61.7	3.7	4.2	26.5	23.1	32.7
Ca	0.2	1.4	4.3	0.6	2.4	0.2
ICP (ppm)						
Ag	18	26	2	3	1	0.6
Ba	110	108	93	88	81	80
Cd	17	40	1	3	<0.5	<0.5
Ga	15	23	3	2.4	1.4	0.4
In	1.5	2.9	0.5	0.5	0.2	<0.1
Pb	120	141	26	27	19	18
Tl	1.9	9.3	2.4	2.0	1.4	0.9
	(n = 6)	(n = 20)	(n = 22)	(n = 23)	(n = 13)	(n = 1)
INAA (ppm)						
Au	1.3	1.1	0.2	0.2	0.1	0.06
As	49	63	41	33	26	43
Co	11	140	260	326	259	420
Cr	8	23	18	27	31	20
Mo	32	117	96	83	74	62
Sb	4.5	4.3	0.7	0.9	0.6	0.5
Se	3	9	12	19	23	29

Notes: n = number of analyses. Cherts and Fe oxides represent the uppermost part, whereas chloritized basalts are the lowermost lithology encountered during drilling.

gold in the upper part of the mound. Chalcopyrite separates show an additional enrichment below 45 mbsf. A similar pattern is obvious for the downhole distribution of As, Sb, and Mo. Down to about 50 mbsf, Au, As, Sb, and Mo values in pyrite separates are generally higher than in bulk samples and chalcopyrite separates. The distribution of Co in bulk samples and chalcopyrite separates shows no downhole trends, whereas the downhole distribution of Co in pyrite separates appears to show a moderate increase with depth to 75 mbsf. Below this, a drop in Co concentrations is apparent followed again by a downhole increase. High Co concentrations (up to 1200 ppm) are caused by the preferred incorporation of Co in the pyrite lattice. The most pronounced difference between bulk samples and pyrite and chalcopyrite separates is documented by the concentration of Se. Bulk samples and, in particular, pyrite separates indicate an increase in concentration downhole. The Se distribution in pyrite separates is similar to the Co distribution and also shows a drop around 75 mbsf with subsequent increase at depth. The chalcopyrite separates, however, have extremely high concentrations (up to 1000 ppm Se) near the top of the mound that significantly drop to lower concentrations within the upper 20 mbsf and reach background values at depth. This is consistent with high Se values found in chalcopyrite-anhydrite-pyrite samples collected with *Alvin* from the Black Smoker Complex (up to 630 ppm Se; Tivey et al., 1995).

TAG-2 Area (Kremlin)

The downhole concentrations of major and trace elements in the TAG-2 area (Kremlin) are shown in Figure 6. Iron and S concentrations are constantly high. The SiO_2 concentrations are high for a chert sample at the top of the mound and for pyrite-silica breccias below 27 mbsf. The Ca peak at 9.3 mbsf corresponds to the presence of anhydrite-cemented pyrite breccias. Striking is the strong enrichment of Cu and Zn, together with Ag, Cd, Pb, Au, Sb, In, and Ga in samples from the surface of the Kremlin area. Thallium is enriched in the uppermost samples and in one sample from deeper in the system. The As concentrations are only insignificantly higher in the upper samples and appear to slightly decrease downhole. The concentrations of Mo are indifferent downhole, whereas Co and Se show an increase in concentration with depth. The change in concentration of some elements at 27 mbsf is caused by the change in lithology from pyrite-anhydrite to pyrite-silica breccias and the associated dilution by silica.

TAG-4 Area

Samples from the west side of the mound are characterized by a good correlation of Fe and S values downhole with the exception of the uppermost Fe oxyhydroxide sample (Fig. 7). The silica distribution strongly increases at 15 mbsf, corresponding to a change in lithology from massive pyrite to pyrite-silica breccias. This effect can be observed in all downhole element profiles in this area. Zinc, Ag, Cd, Pb, Ga, and Tl are enriched near the surface, whereas Cu and Co are enriched below this depth. The concentrations of Au, As, and Sb also largely mirror the downhole distribution of Zn. TAG-4 is the only area in which a downhole increase instead of a decrease of Cu is observed. Indium concentrations appear to follow the depth profile of Cu. The depth profiles of Ga and Cd are largely similar and follow the Zn distribution downhole. This is explained by the preferred incorporation of Ga and Cd in sphalerite.

TAG-5 Area

In samples from the northern part of the mound, Fe and S values are well correlated, similar to other areas (Fig. 8). Silica concentrations increase downhole because of the presence of silica in silicified wallrock breccias and chloritized and paragonitized basalts, whereas Ca concentrations are enriched in anhydrite veins and pyrite-anhydrite breccias occurring close to the seafloor in this area. Copper and Zn show a general decrease in concentration downhole, but are somewhat enriched in massive pyrite samples occurring between 10 and 20 mbsf. The depth profiles of Ag, Cd, Pb, Au, In, Ga, and to some extent, Sb, As, and Tl, largely follow the downhole distribution of Cu and Zn. Indium and Ga profiles show analogies to the depth profile of Ag, whereas the Mo distribution is somewhat similar to Fe. Cobalt appears to increase in concentration downhole, whereas the Se distribution is more erratic.

Element Correlations and Correlation Coefficients

A correlation matrix for all bulk samples analyzed from the TAG-1 to TAG-5 areas (Fig. 9) indicates a statistically significant correlation (99% confidence level) of the elements Zn, Ag, Au, Sb, In, Ga, Pb, and Cd, which are typically of submarine massive sulfides of low-temperature hydrothermal origin (cf. Hannington et al., 1991).

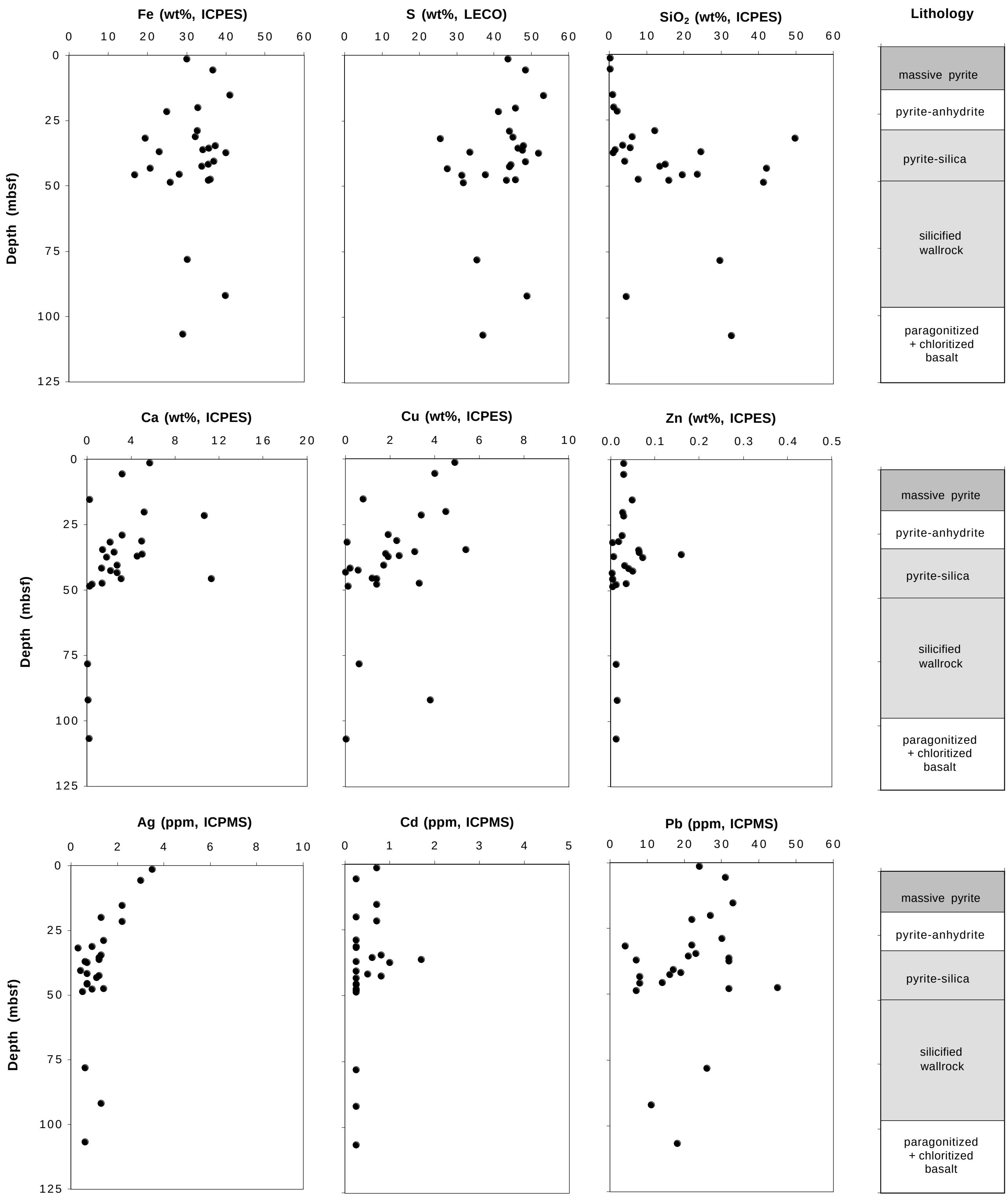

Figure 4. Downhole distribution of selected major and trace elements in bulk sulfide samples from the TAG-1 area (Black Smoker Complex: Holes 957C, 957E, 957F, and 957G).

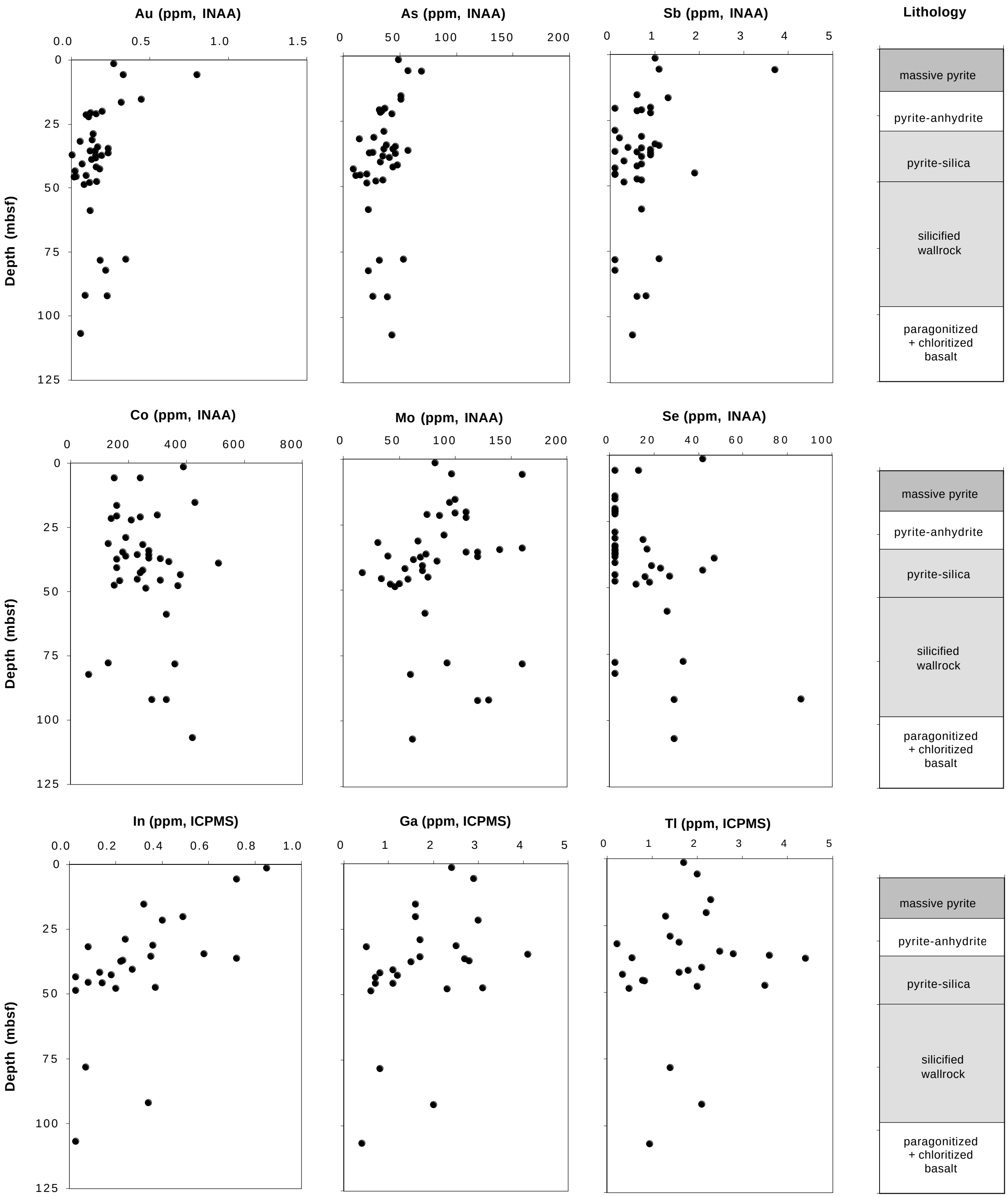

Figure 4 (continued).

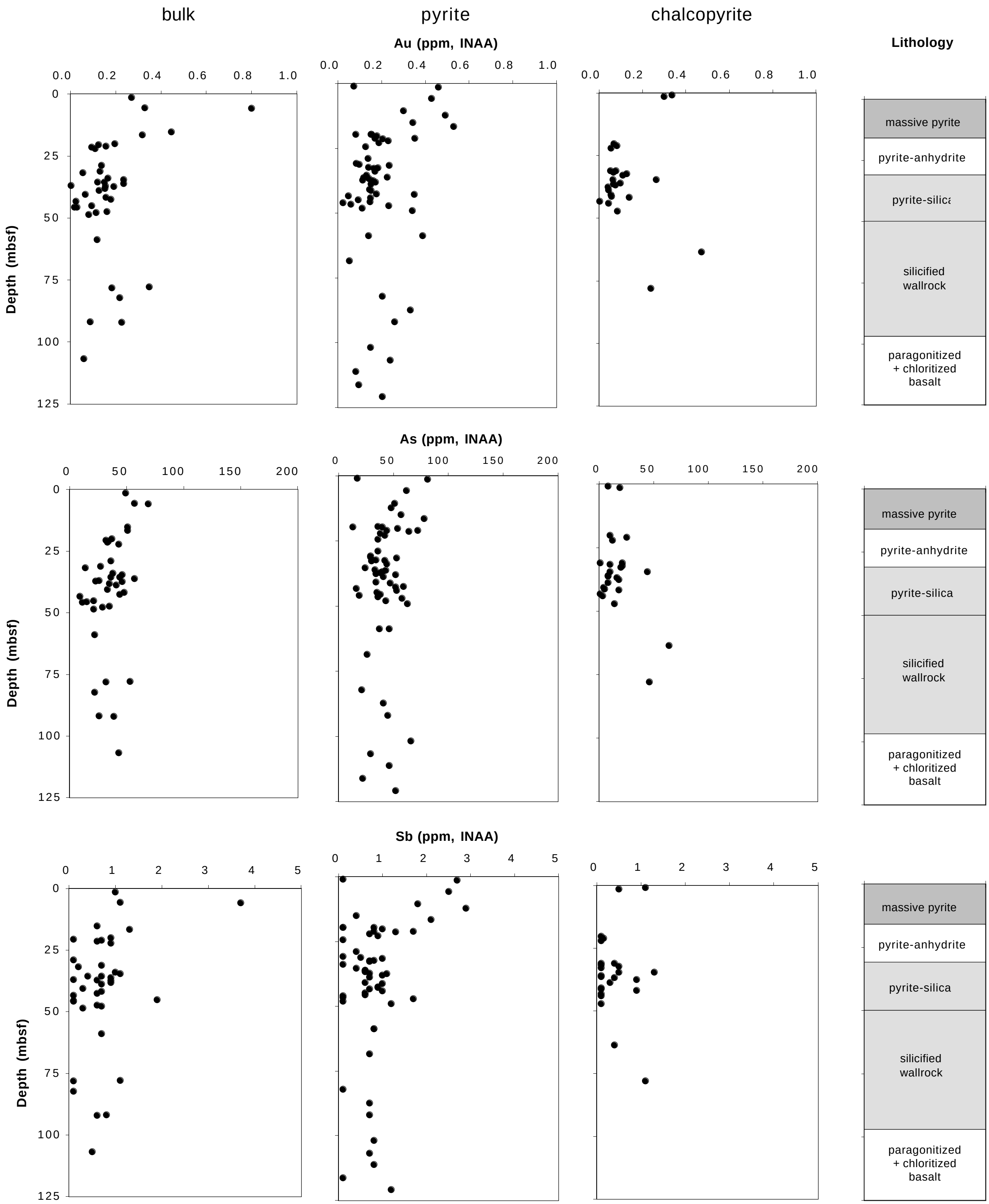

Figure 5. Comparison of the downhole distribution of selected trace elements in bulk sulfide samples (left), pyrite separates (center), and chalcopyrite separates (right) from the TAG-1 area (Black Smoker Complex: Holes 957C, 957E, 957F, and 957G).

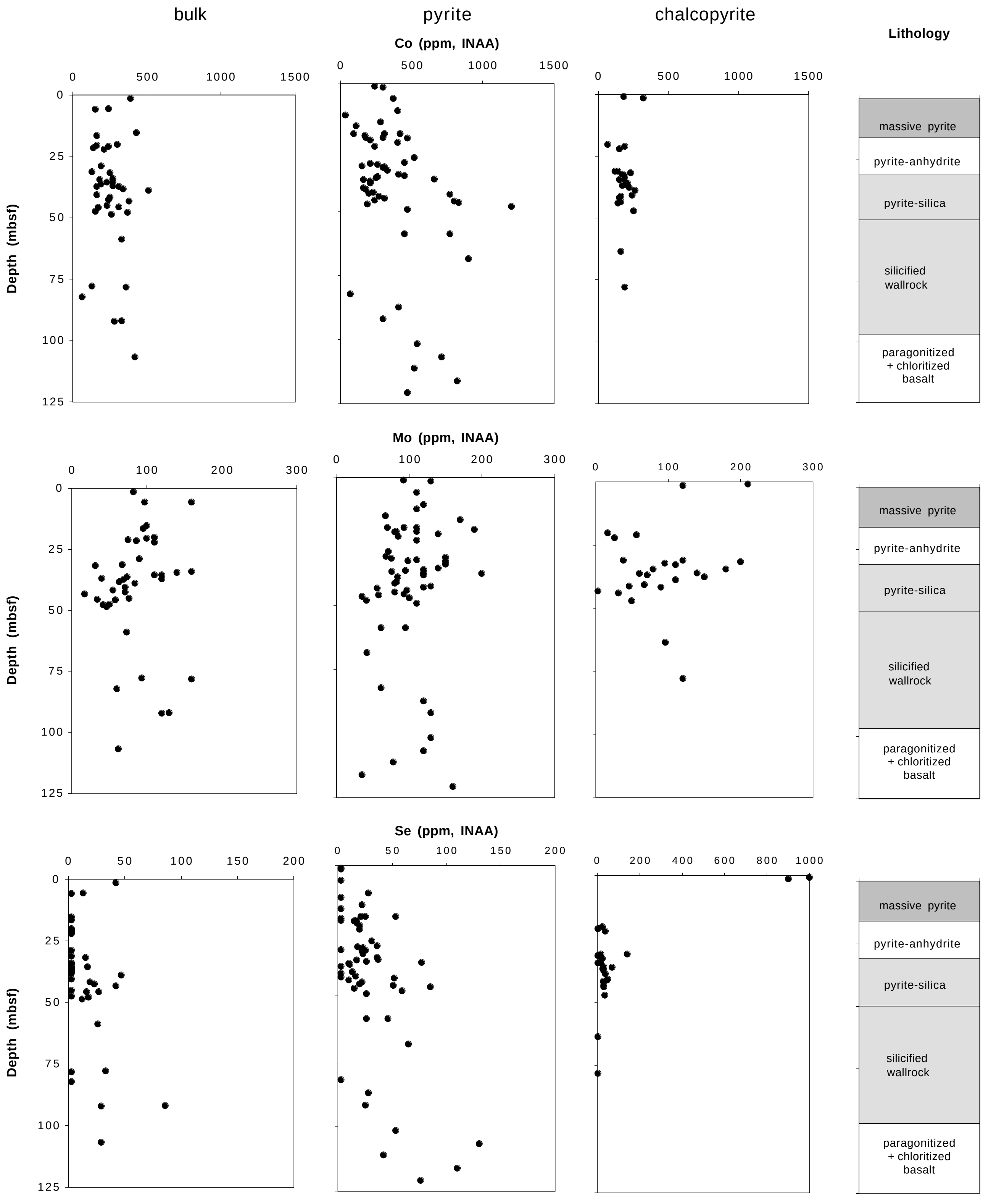

Figure 5 (continued).

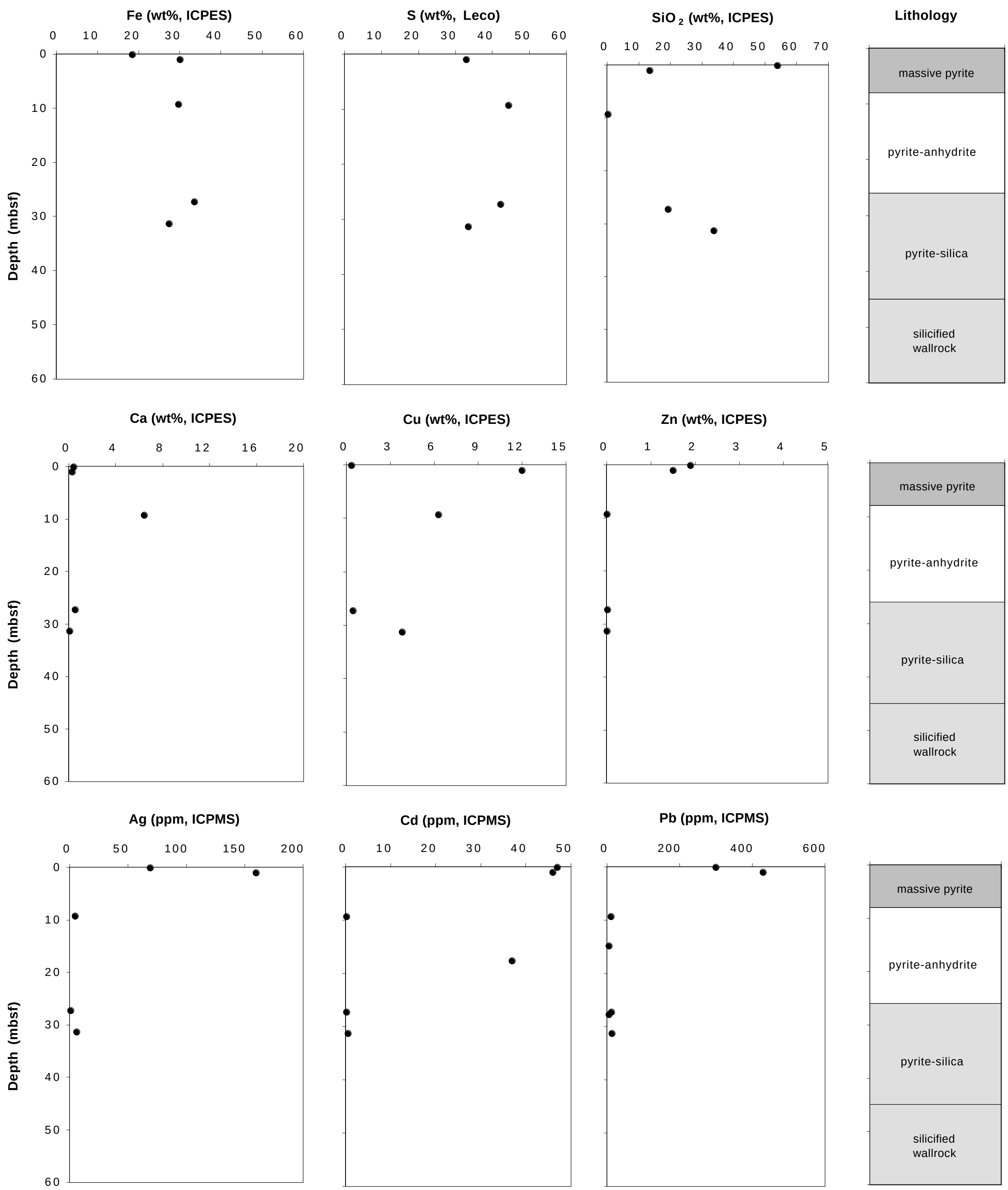

Figure 6. Downhole distribution of selected major and trace elements in bulk sulfide samples from the TAG-2 area (Kremlin area: Holes 957A, 957B, 957H, and 957N).

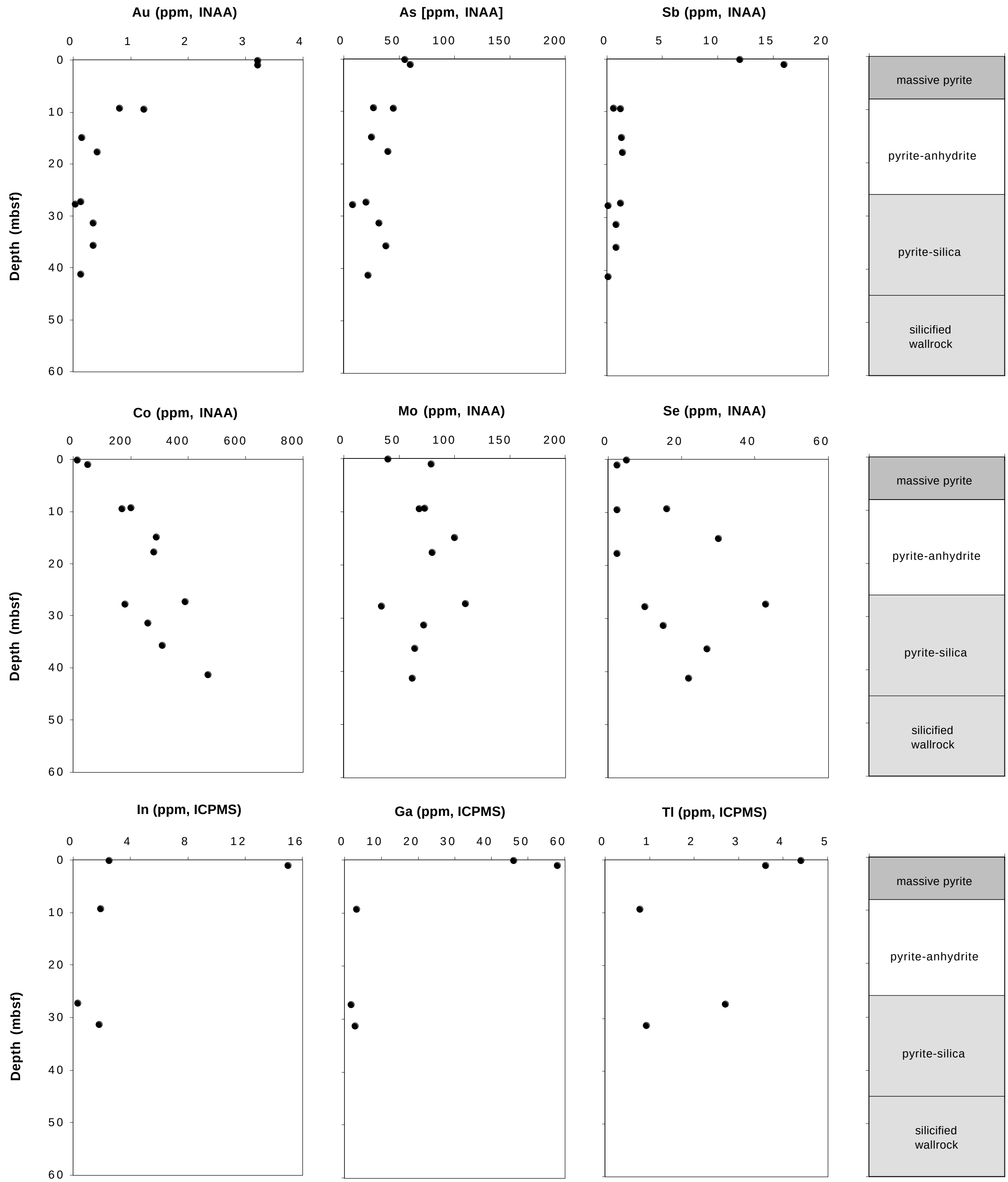

Figure 6 (continued).

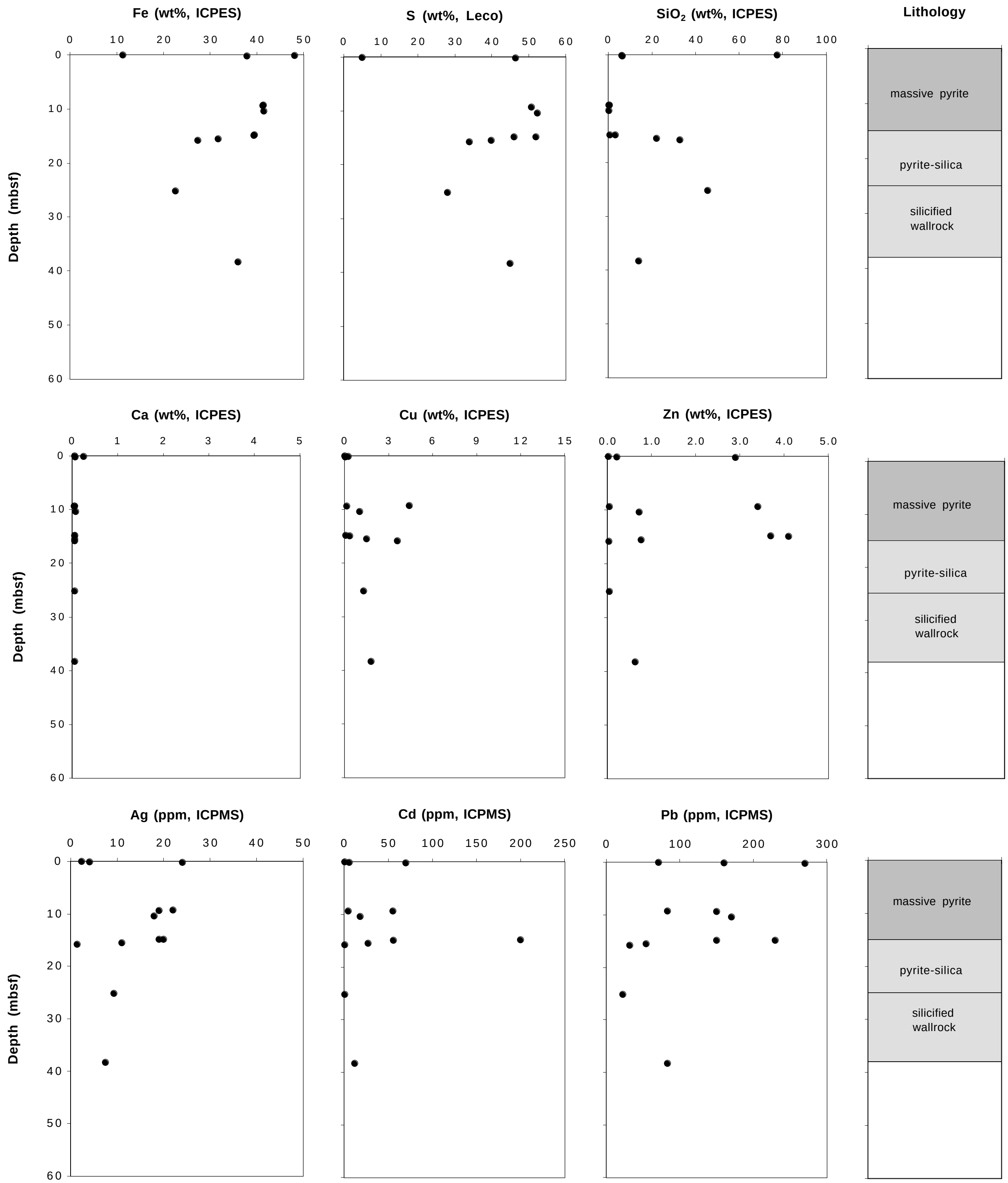

Figure 7. Downhole distribution of selected major and trace elements in bulk sulfide samples from the TAG-4 area (west side of the mound: Holes 957I, 957J, 957K, and 957M).

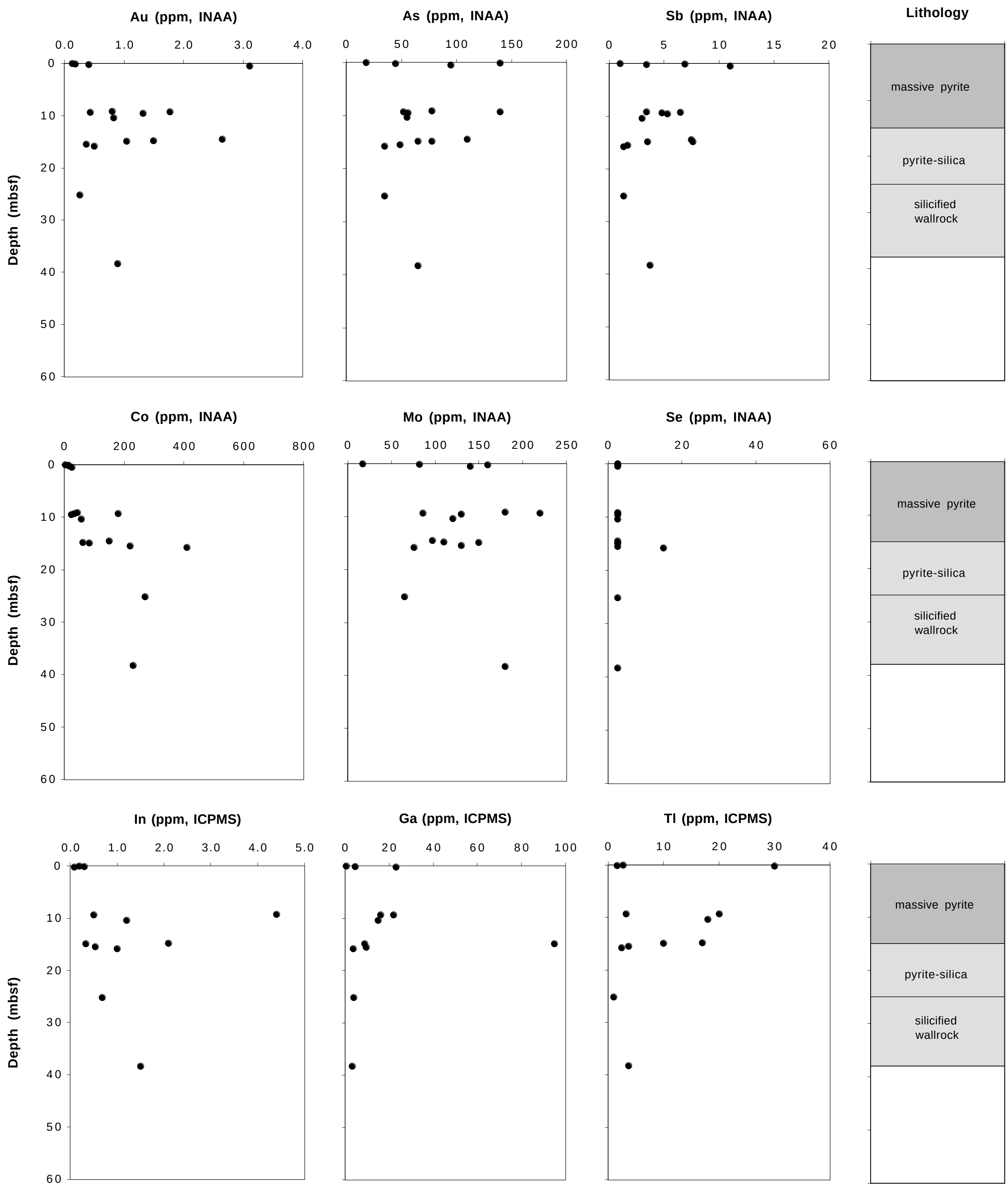

Figure 7 (continued).

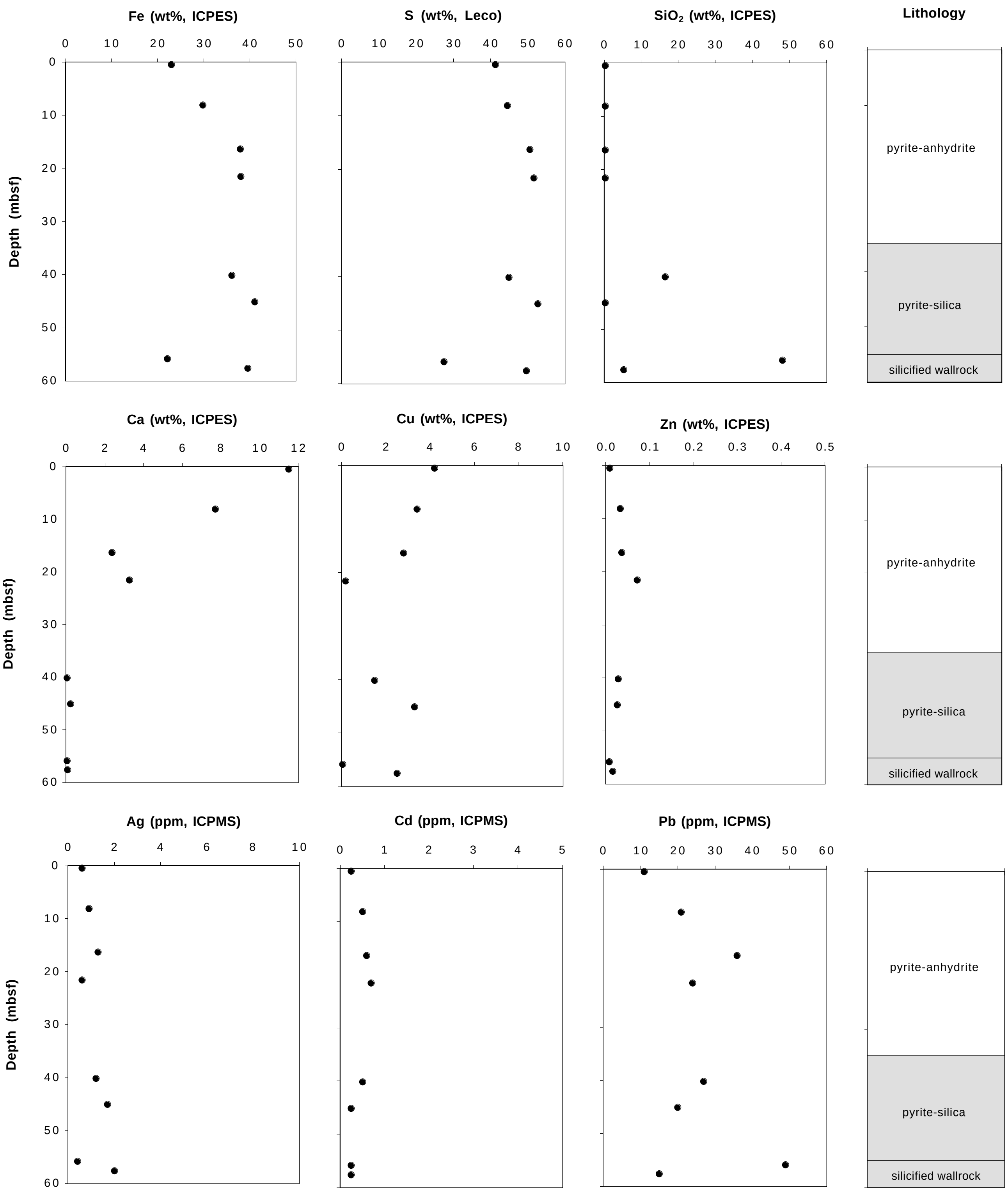

Figure 8. Downhole distribution of selected major and trace elements in bulk sulfide samples from the TAG-5 area (north side of the mound: Holes 957O, 957P).

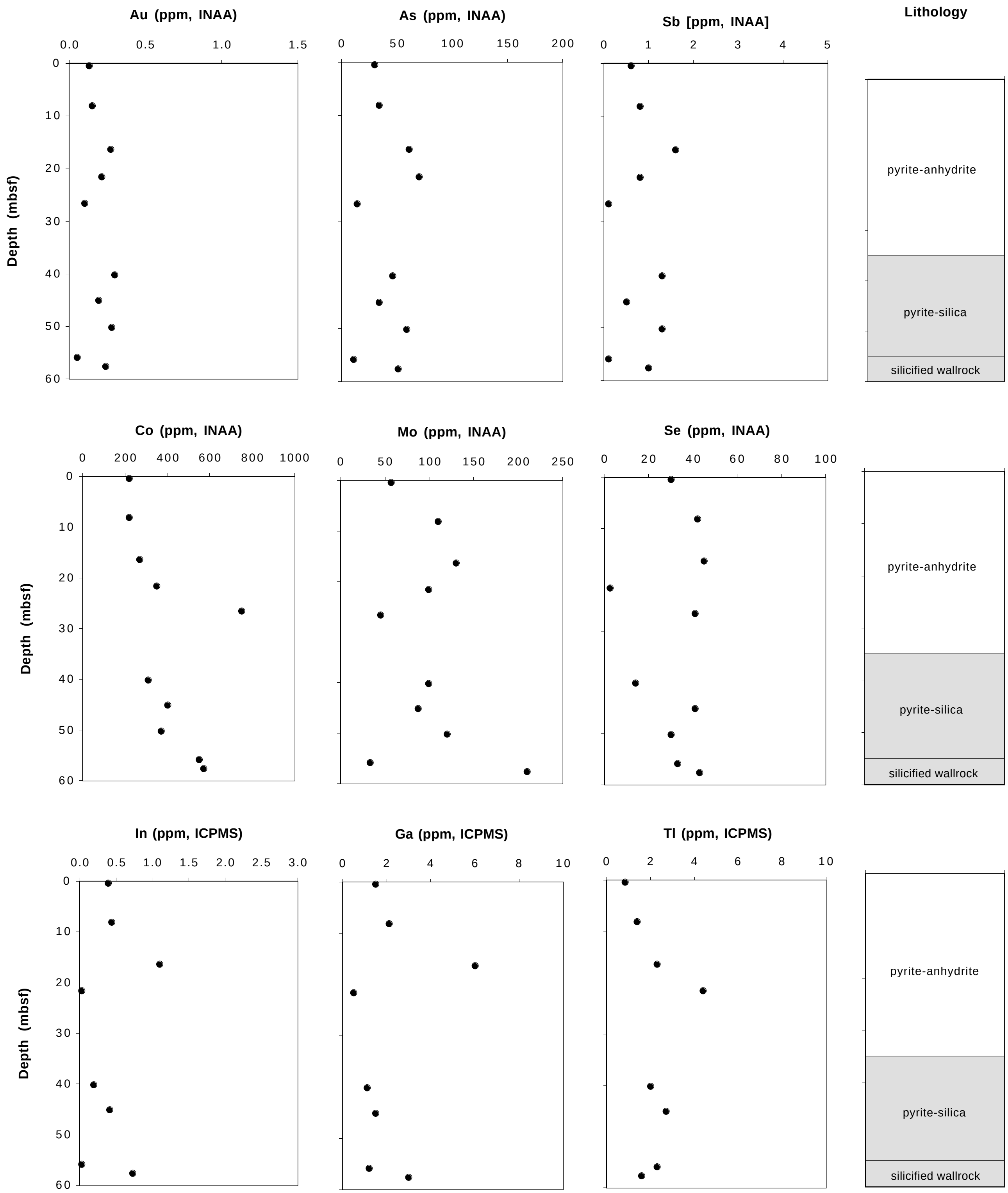

Figure 8 (continued).

The best correlations within this group of elements occur for Ag/In (r = 0.92, n = 57), Pb/Sb (r = 0.92, n = 57), Ga/Cd (r = 0.91, n = 37), and Au/Sb (r = 0.89, n = 85). The most significant correlation of the entire data set is found for Sr/Ca (r = 0.98, n = 36) and is explained by the preferred substitution of Sr for Ca in anhydrite. A correlation coefficient of r = 0.87 (n = 37) for Zn/Cd and r = 0.72 (n = 57) for Zn/Tl indicates the presence of Cd and Tl in the sphalerite lattice.

The correlation coefficients (99% confidence level) of particular element pairs show significant differences when compared for the TAG-1, -2,- 4, and -5 areas (Fig. 10). This is also obvious from Table 5, which compares selected element correlations for these areas. In the TAG-1 area, a good correlation within the low-temperature group of elements is obvious. Silica is clearly negatively correlated with this group of elements (Zn, Au, Ag, As, Sb, Tl, Ga, In, and Pb), as well as with Cu, Fe, and S. The strong affinity of Sr and Ca in anhydrite, Fe and S in pyrite, and Zn and Cd in sphalerite is documented by correlation coefficients of r = 0.98 (Sr/Ca, n = 20), r = 0.93 (Fe/S, n = 25), and r = 0.92 (Zn/Cd, n = 9). In the TAG-1 area, Cu correlates positively with Ag, Ga, In, Mo, and Sb.

In the TAG-2 area, only a limited number of samples were analyzed for all elements. However, a positive correlation of the low-temperature element association can also be recognized.

The correlation matrix for the samples from the TAG-4 area indicates that the correlation among the low-temperature suite of elements is less pronounced. In particular, the Au/Ag, Au/Pb, Au/Zn correlations as well as the correlation of In and Ga with other elements of this group, do not exist. Significant correlations occur for Ca/V (0.97, n = 9), Ba/Ca (r = 0.96, n = 12), Cd/Ga (0.94, n = 13), Ba/V (0.92, n = 9), Pb/Tl (0.86, n = 13), and Fe/SiO_2 (r = –0.97, n = 12). In contrast to other areas, a negative correlation of Cu with Ag and Sb is observed.

Elemental correlations for samples originating from the TAG-5 area show a number of close similarities with those of the TAG-1 area. The correlation among elements of the low-temperature association is even better developed as in the TAG-1 area. However, the coefficients for the correlation of Fe, S, and SiO_2 are insignificant. Clearly outstanding are the Zn/Cd (r = 0.99, n = 7), In/Ga (r = 99, n = 10), and Sr/Ca (r = 0.99, n = 10) correlations. Among other pairs, In/Ag (r = 0.98, n = 10), Cd/In (r = 0.97, n = 7), Zn/In (r = 0.96, n = 10), Cd/Ag (r = 0.96, n = 10), Zn/Ag (r = 0.96, n = 10); Cu/In (r = 0.95, n = 10), Au/Ag (r = 0.95, n = 10); and Ga/Ag (r = 0.95, n = 10) also show statistically significant correlations.

The good positive correlation of Cu with Au, Ag, Sb, Cd, In, and Ga is not typical for seafloor hydrothermal systems, whereas elements of the low-temperature assemblage are found to correlate well in many other seafloor hydrothermal sites (cf. Hannington et al., 1991).

SULFUR ISOTOPES

Forty-nine bulk samples from the TAG-1 to TAG-5 areas were investigated for their sulfur-isotopic ratios. The average $\delta^{34}S$ values of duplicate analyses are given in Table 6, together with a description of the samples analyzed. All $\delta^{34}S$ ratios are within a narrow interval of +4.6‰ to +8.2‰, with an average of +6.4‰ $\delta^{34}S$ (n = 49; Fig. 11). The average sulfur-isotope ratios for the TAG-1 to TAG-5 areas are only insignificantly different from each other, ranging from +6.6‰ at TAG-2 to +6.2‰ at TAG-5 (Table 7). The average $\delta^{34}S$ ratios for samples from the massive pyrite zone (+5.8‰) and the pyrite-anhydrite zone (+5.9‰) are nearly 1‰ depleted compared to the footwall lithologies, averaging +6.8‰ and +6.7‰ respectively (Table 7).

An increase in the sulfur-isotopic ratio downhole is not obvious in all areas, but is distinct in the depth profiles for the TAG-2 and TAG-4 areas (Fig. 12).

The average $\delta^{34}S$ ratios of sulfides from the TAG mound are about 3‰ higher than the average $\delta^{34}S$ ratio of sulfides from any other hydrothermal system at sediment-free mid-ocean ridges (Fig. 13). Similar high sulfur-isotopic ratios have so far only been reported from sediment-hosted massive sulfide deposits at the mid-ocean ridges or backarc spreading centers in the southwest Pacific. Here, elevated $\delta^{34}S$ values are explained by the contribution of seawater sulfate (+21‰) either through sediments filling the active rift valley and reacting with the upwelling hydrothermal fluids (sedimented mid-ocean ridges) or through subducted sediments and the formation of backarc volcanics with elevated initial $\delta^{34}S$ values (backarc rifts).

DISCUSSION

Humphris et al. (1995) and Hannington et al. (Chap. 28, this volume) have pointed out that the internal structure of the TAG mound bears striking similarities to ancient volcanic-hosted massive sulfide deposits preserved in ophiolites, such as the Troodos ophiolite in Cyprus, the Semail ophiolite in Oman, and the Bay of Islands ophiolite in Newfoundland. Similarities between the TAG mound and ancient ophiolitic massive sulfide deposits include the abundance and types of breccia ores and sulfide conglomerates, the occurrence of Fe-bearing cherts, and the size as deduced from the results of drilling. The major- and trace-element geochemistry and the metal distribution within the TAG mound strongly support this analogy.

Similar to the massive pyrite and massive pyrite breccias of the TAG mound, massive ore of the sulfide deposits in the Troodos ophiolite contains more than 40 wt% S and is underlain by a pyrite-silica zone (i.e., pyrite-silica breccia) with 30–40 wt% S and high SiO_2 contents, representing the top of the stockwork zone. The stockwork it-

		85	57	85	54	37	85	77	57	57	85	57	85	41	36	57	78	40	57	57	57	50	50
		Au	Ag	As	Ba	Cd	Co	Cr	Ga	In	Mo	Pb	Sb	Se	Sr	Tl	U	V	Cu	Fe	Zn	S	SiO_2
57	Ag	0.784	1																				
85	As	0.519	0.216	1																			
54	Ba	-0.113	-0.051	0.567	1																		
37	Cd	0.477	0.594	0.278	-0.044	1																	
85	Co	-0.447	-0.344	-0.242	-0.049	-0.395	1																
77	Cr	-0.110	-0.033	-0.236	-0.105	-0.063	-0.017	1															
57	Ga	0.719	0.776	0.330	-0.058	0.907	-0.427	0.063	1														
57	In	0.762	0.924	0.310	-0.064	0.518	-0.234	-0.027	0.742	1													
85	Mo	0.081	0.037	0.468	0.339	0.241	0.009	-0.178	0.076	0.021	1												
57	Pb	0.771	0.866	0.430	0.013	0.734	-0.501	-0.086	0.844	0.813	0.203	1											
85	Sb	0.886	0.873	0.614	0.190	0.558	-0.462	-0.098	0.779	0.757	0.209	0.916	1										
41	Se	-0.261	-0.191	-0.157	0.016	-0.226	0.604	0.029	-0.220	-0.079	0.035	-0.286	-0.254	1									
36	Sr	-0.259	-0.144	-0.181	-0.057	-0.208	0.014	-0.115	-0.213	-0.136	-0.092	-0.248	-0.247	0.115	1								
57	Tl	0.183	0.148	0.257	-0.063	0.593	-0.349	-0.072	0.399	0.055	0.494	0.453	0.328	-0.203	-0.212	1							
78	U	0.405	0.160	0.443	0.141	0.059	-0.024	0.051	0.153	0.224	0.278	0.145	0.358	-0.129	-0.234	-0.049	1						
40	V	0.631	0.671	0.152	0.231	0.281	-0.320	0.382	0.548	0.641	-0.150	0.680	0.751	-0.155	-0.186	-0.069	0.199	1					
57	Cu	0.328	0.517	0.257	-0.097	0.154	0.079	-0.092	0.361	0.721	0.191	0.393	0.272	0.244	0.129	-0.085	0.124	0.287	1				
57	Fe	-0.103	-0.102	0.599	0.293	0.053	0.255	-0.242	-0.056	-0.103	0.668	0.071	0.119	0.136	-0.128	0.303	0.268	-0.045	-0.022	1			
57	Zn	0.455	0.567	0.275	-0.039	0.874	-0.449	-0.045	0.734	0.440	0.403	0.742	0.559	-0.263	-0.232	0.715	0.011	0.276	0.091	0.117	1		
50	S	0.071	-0.122	0.009	-0.494	0.086	0.003	-0.126	0.022	-0.071	0.458	-0.125	-0.132	0.078	0.056	0.321	0.140	-0.500	0.141	0.091	0.117	1	
50	SiO_2	0.153	0.041	-0.479	-0.126	-0.062	-0.229	0.042	-0.009	-0.028	-0.628	-0.054	-0.034	-0.198	-0.296	-0.266	-0.179	0.062	-0.326	-0.793	-0.106	-0.474	1
57	Ca	-0.277	-0.146	-0.207	-0.086	-0.216	0.006	-0.117	-0.219	-0.145	-0.117	-0.261	-0.268	0.063	0.977	-0.217	-0.249	-0.203	0.102	-0.143	-0.240	0.085	-0.288

Figure 9. Correlation matrix for the total of samples analyzed from the TAG mound. Correlation coefficients with 99% confidence level are highlighted. The number of samples analyzed is given above and beside the respective element.

TAG-1

		40	25	40	25	9	40	40	25	25	40	25	40	17	20	25	33	16	25	25	25	25	22
		Au	Ag	As	Ba	Cd	Co	Cr	Ga	In	Mo	Pb	Sb	Se	Sr	Tl	U	V	Cu	Fe	Zn	S	SiO_2
25	Ag	0.658	1																				
40	As	0.757	0.523	1																			
25	Ba	0.678	0.286	0.629	1																		
9	Cd	0.455	0.228	0.606	0.282	1																	
40	Co	-0.163	0.158	-0.093	0.139	-0.209	1																
40	Cr	-0.165	-0.143	-0.240	-0.205	-0.143	0.305	1															
25	Ga	0.368	0.510	0.411	0.290	0.324	-0.378	-0.426	1														
25	In	0.614	0.764	0.638	0.357	0.482	-0.178	-0.364	0.748	1													
40	Mo	0.516	0.308	0.489	0.499	0.169	-0.037	-0.148	0.318	0.408	1												
25	Pb	0.669	0.426	0.658	0.563	0.326	-0.119	-0.174	0.486	0.489	0.327	1											
40	Sb	0.766	0.554	0.602	0.556	0.481	-0.149	-0.377	0.591	0.752	0.448	0.518	1										
17	Se	-0.171	0.138	-0.147	0.025	-0.188	0.482	0.399	-0.218	-0.062	-0.099	-0.403	-0.093	1									
20	Sr	-0.144	0.334	-0.122	-0.462	0.144	-0.343	-0.284	0.253	0.377	-0.083	-0.132	0.000	-0.137	1								
25	Tl	0.533	0.201	0.645	0.676	0.595	-0.325	-0.279	0.452	0.503	0.361	0.761	0.634	-0.222	-0.146	1							
33	U	0.288	0.531	0.395	0.401	-0.048	0.034	-0.002	0.451	0.421	0.208	0.438	0.074	-0.134	0.027	0.113	1						
16	V	0.041	0.177	-0.085	0.288	-0.190	0.192	0.265	0.102	0.027	0.066	-0.125	-0.050	0.218	-0.026	-0.024	0.283	1					
25	Cu	0.324	0.600	0.342	0.294	0.137	-0.251	-0.469	0.789	0.811	0.514	0.356	0.626	0.030	0.361	0.416	0.312	0.077	1				
25	Fe	0.639	0.254	0.701	0.931	0.316	-0.025	-0.218	0.335	0.393	0.500	0.665	0.631	-0.018	-0.502	0.777	0.341	0.111	0.341	1			
25	Zn	0.489	0.163	0.681	0.424	0.922	-0.312	-0.177	0.377	0.535	0.249	0.482	0.508	-0.278	0.022	0.747	0.020	-0.138	0.202	0.490	1		
25	S	0.675	0.418	0.753	0.878	0.434	-0.187	-0.417	0.486	0.582	0.502	0.701	0.702	-0.110	-0.159	0.818	0.423	0.118	0.505	0.928	0.577	1	
22	SiO_2	-0.594	-0.568	-0.665	-0.672	-0.445	0.315	0.497	-0.641	-0.752	-0.502	-0.642	-0.693	0.138	-0.249	-0.740	-0.421	-0.139	-0.705	-0.707	-0.542	-0.908	1
25	Ca	-0.198	0.249	-0.171	-0.470	0.131	-0.433	-0.290	0.241	0.291	-0.115	-0.140	-0.052	-0.184	0.983	-0.153	0.008	-0.019	0.288	-0.510	0.019	-0.166	-0.232

TAG-2

		13	5	13	5	5	13	13	5	5	13	5	13	13	5	5	13	5	5	5	5	5	5
		Au	Ag	As	Ba	Cd	Co	Cr	Ga	In	Mo	Pb	Sb	Se	Sr	Tl	U	V	Cu	Fe	Zn	S	SiO_2
5	Ag	0.874	1																				
13	As	0.855	0.905	1																			
5	Ba	-0.672	-0.244	-0.606	1																		
5	Cd	0.987	0.876	0.965	-0.666	1																	
13	Co	-0.831	-0.756	-0.674	0.736	-0.893	1																
13	Cr	-0.221	0.101	-0.516	0.612	-0.170	-0.044	1															
5	Ga	0.978	0.945	0.973	-0.539	0.985	-0.876	-0.092	1														
5	In	0.677	0.940	0.745	0.069	0.663	-0.581	0.230	0.780	1													
13	Mo	-0.211	-0.251	0.004	0.898	-0.571	0.340	-0.106	-0.481	-0.035	1												
5	Pb	0.960	0.968	0.963	-0.469	0.969	-0.846	-0.029	0.997	0.824	-0.417	1											
13	Sb	0.948	0.956	0.780	-0.497	0.978	-0.736	-0.068	0.998	0.798	-0.103	0.999	1										
13	Se	-0.577	-0.673	-0.566	0.574	-0.714	0.693	0.267	-0.727	-0.592	0.541	-0.706	-0.452	1									
5	Sr	-0.286	-0.358	-0.399	0.212	-0.428	0.098	-0.643	-0.402	-0.221	0.014	-0.412	-0.431	0.035	1								
5	Tl	0.794	0.669	0.717	-0.596	0.866	-0.583	0.029	0.817	0.403	-0.294	0.801	0.827	-0.279	-0.589	1							
13	U	0.813	0.982	0.819	-0.403	0.931	-0.755	-0.310	0.976	0.880	-0.183	0.985	0.704	-0.733	-0.386	0.694	1						
5	V	0.938	0.985	0.945	-0.393	0.944	-0.818	0.011	0.986	0.869	-0.355	0.996	0.992	-0.691	-0.388	0.767	0.989	1					
5	Cu	0.361	0.673	0.441	0.341	0.288	-0.382	0.096	0.437	0.867	0.068	0.488	0.446	-0.528	0.199	-0.080	0.596	0.553	1				
5	Fe	-0.597	-0.182	-0.579	0.974	-0.588	0.709	0.580	-0.464	0.102	0.945	-0.395	-0.418	0.627	0.235	-0.460	-0.359	-0.318	0.326	1			
5	Zn	0.976	0.802	0.939	-0.758	0.990	-0.893	-0.243	0.953	0.554	-0.637	0.926	0.940	-0.695	-0.425	0.882	0.875	0.890	0.166	-0.678	1		
5	S	-0.528	-0.610	-0.731	0.452	-0.605	0.507	-0.544	-0.600	-0.619	0.381	-0.603	-0.599	0.611	0.722	-0.328	-0.675	-0.588	-0.483	0.558	-0.598	1	
5	SiO_2	0.353	0.051	0.387	-0.774	0.437	-0.340	-0.058	0.307	-0.233	-0.603	0.255	0.289	-0.244	-0.683	0.531	0.198	0.177	-0.590	-0.813	0.525	-0.628	1
5	Ca	-0.257	-0.353	-0.379	0.164	-0.399	0.069	-0.678	-0.381	-0.233	-0.022	-0.394	-0.411	0.021	0.999	-0.556	-0.375	-0.374	0.174	0.193	-0.390	0.728	-0.652

TAG-4

		17	13	17	12	13	17	13	13	13	17	13	17	2	2	13	16	9	13	13	13	10	12
		Au	Ag	As	Ba	Cd	Co	Cr	Ga	In	Mo	Pb	Sb	Se	Sr	Tl	U	V	Cu	Fe	Zn	S	SiO_2
13	Ag	0.611	1																				
17	As	0.553	0.339	1																			
12	Ba	-0.187	-0.131	0.588	1																		
13	Cd	0.461	0.529	0.095	-0.021	1																	
17	Co	-0.100	-0.337	-0.145	-0.259	-0.331	1																
13	Cr	-0.055	0.286	-0.221	-0.128	-0.008	0.259	1															
13	Ga	0.604	0.500	0.241	-0.071	0.937	-0.237	-0.146	1														
13	In	0.851	0.356	0.587	-0.252	0.116	0.247	-0.275	0.388	1													
17	Mo	0.180	0.630	0.197	0.147	0.336	-0.187	0.551	0.171	-0.010	1												
13	Pb	0.287	0.698	0.318	0.319	0.686	-0.652	-0.027	0.592	-0.040	0.519	1											
17	Sb	0.816	0.527	0.777	0.482	0.546	-0.360	-0.124	0.629	0.515	0.317	0.629	1										
2	Se	-	-	-	-	-	-	-	-	-	-	-	-	1									
2	Sr	-	-	-	-	-	-	-	-	-	-	-	-	-	1								
13	Tl	0.163	0.753	-0.055	-0.069	0.591	-0.505	0.279	0.466	-0.124	0.617	0.859	0.303	-	-	1							
16	U	0.549	-0.120	0.403	0.068	-0.173	0.459	0.151	-0.043	0.514	0.077	-0.286	0.391	-	-	-0.405	1						
9	V	-0.284	-0.306	0.593	0.924	-0.224	-0.200	-0.257	-0.192	-0.169	-0.136	0.086	0.387	-	-	-0.306	0.061	1					
13	Cu	0.444	-0.022	0.324	-0.250	-0.382	0.754	-0.056	-0.159	0.709	-0.085	-0.457	0.024	-	-	-0.402	0.573	-0.146	1				
13	Fe	0.489	0.639	0.766	0.573	0.342	-0.199	0.170	0.341	0.306	0.692	0.657	0.812	-	-	0.453	0.206	0.362	0.092	1			
13	Zn	0.319	0.690	0.022	0.021	0.777	-0.430	0.260	0.558	-0.143	0.651	0.718	0.411	-	-	0.729	-0.338	-0.270	-0.475	0.448	1		
10	S	0.624	0.705	-0.578	-0.760	0.489	-0.148	0.373	0.409	0.378	0.609	0.324	-0.077	-	-	0.638	-0.052	-0.888	-0.131	-0.013	0.591	1	
12	SiO_2	-0.587	-0.752	-0.665	-0.389	-0.436	0.131	-0.268	-0.425	-0.359	-0.767	-0.670	-0.764	-	-	-0.546	-0.219	-0.146	-0.135	-0.973	-0.547	-0.393	1
13	Ca	-0.279	-0.220	0.581	0.959	-0.139	-0.325	-0.276	-0.137	-0.229	-0.043	0.257	0.435	-	-	-0.125	-0.045	0.971	-0.234	0.451	-0.145	-0.799	-0.240

TAG-5

		12	10	12	10	7	12	12	10	10	12	10	12	12	8	10	12	6	10	10	10	10	6
		Au	Ag	As	Ba	Cd	Co	Cr	Ga	In	Mo	Pb	Sb	Se	Sr	Tl	U	V	Cu	Fe	Zn	S	SiO_2
10	Ag	0.953	1																				
12	As	0.761	0.592	1																			
10	Ba	0.879	0.913	0.639	1																		
7	Cd	0.891	0.964	0.549	0.944	1																	
12	Co	-0.394	-0.229	-0.510	-0.316	-0.323	1																
12	Cr	0.158	0.677	-0.299	0.689	0.737	0.566	1															
10	Ga	0.902	0.949	0.596	0.917	0.951	-0.321	0.676	1														
10	In	0.925	0.977	0.596	0.929	0.969	-0.320	0.662	0.992	1													
12	Mo	0.488	0.331	0.680	0.324	0.199	-0.164	-0.266	0.338	0.338	1												
10	Pb	0.766	0.847	0.389	0.803	0.896	-0.138	0.878	0.874	0.856	0.011	1											
12	Sb	0.894	0.806	0.837	0.846	0.799	-0.585	-0.052	0.873	0.857	0.599	0.673	1										
12	Se	0.108	0.251	-0.201	0.061	0.093	0.197	0.185	0.307	0.289	0.229	0.111	0.016	1									
8	Sr	-0.371	-0.311	-0.309	-0.322	-0.217	-0.594	-0.557	-0.237	-0.222	-0.301	-0.409	-0.248	-0.010	1								
10	Tl	0.579	0.514	0.661	0.468	0.468	0.053	0.343	0.401	0.419	0.092	0.525	0.357	-0.207	-0.562	1							
12	U	-0.007	-0.144	0.092	-0.015	-0.256	0.111	-0.198	-0.185	-0.176	0.580	-0.339	0.077	0.141	-0.455	-0.262	1						
6	V	0.159	0.208	0.147	0.208	0.181	0.489	0.419	0.362	0.293	0.550	0.296	0.282	0.417	-0.421	-0.089	0.365	1					
10	Cu	0.866	0.934	0.481	0.855	0.907	-0.445	0.489	0.917	0.949	0.270	0.710	0.767	0.368	-0.005	0.276	-0.189	0.101	1				
10	Fe	-0.134	-0.337	0.270	-0.300	-0.508	0.285	-0.492	-0.406	-0.402	0.460	-0.537	-0.126	0.058	-0.366	0.195	0.569	-0.043	-0.416	1			
10	Zn	0.909	0.963	0.617	0.944	0.994	-0.335	0.705	0.940	0.960	0.217	0.886	0.808	0.053	-0.236	0.551	-0.281	0.139	0.891	-0.445	1		
10	S	0.290	0.106	0.665	0.219	-0.013	-0.210	-0.397	0.071	0.093	0.608	-0.265	0.338	0.052	-0.127	0.314	0.389	-0.113	0.130	0.754	0.056	1	
6	SiO_2	-0.325	-0.208	-0.598	-0.289	-0.145	0.562	0.459	-0.215	-0.247	-0.484	0.215	-0.405	-0.121	-0.330	-0.107	-0.082	0.227	-0.379	-0.375	-0.193	-0.855	1
10	Ca	-0.366	-0.322	-0.252	-0.320	-0.222	-0.599	-0.596	-0.242	-0.229	-0.319	-0.416	-0.240	-0.080	0.989	-0.510	-0.482	-0.418	-0.024	-0.351	-0.234	-0.096	-0.353

Figure 10. Correlation matrix for samples analyzed from the TAG-1, -2, -4, and -5 areas. Correlation coefficients with 99% confidence level are highlighted. The number of samples analyzed is given above and beside the respective element. Dashes indicate insufficient number of analyses to calculate correlation factors.

Table 5. Statistically significant element correlations for Au, Zn, Cu, and other elements based on the chemical composition of drill core samples from the TAG mound.

	TAG-1	TAG-2	TAG-4	TAG-5
Gold	Au/Sb	Au/Sb	Au/Sb	Au/Sb
	Au/As	Au/As	(Au/As)	Au/As
	Au/In	—	Au/In	Au/In
	Au/Pb	Au/Pb	—	Au/Pb
	Au/Ag	—	—	Au/Ag
	—	Au/Zn	—	Au/Zn
	—	Au/Ga	—	Au/Ga
	—	—	—	Au/Cu
Zinc	Zn/Cd	Zn/Cd	Zn/Cd	Zn/Cd
	Zn/In	—	—	Zn/In
	—	—	Zn/Ag	Zn/Ag
	—	(Zn/Sb)	—	Zn/Sb
	Zn/As	(Zn/As)	—	—
	—	(Zn/Ga)	—	Zn/Ga
Copper	Cu/In	—	Cu/In	Cu/In
	Cu/Ag	—	—	Cu/Ag
	Cu/Ga	—	—	Cu/Ga
	—	—	Cu/Co	—
	—	—	—	Cu/Au
Others	Sr/Ca	Sr/Ca	Sr/Ca	Sr/Ca
	As/Sb	As/Sb	As/Sb	As/Sb
	Pb/Sb	Pb/Sb	—	Pb/Sb
	—	Cd/Sb	Cd/Sb	Cd/Sb
	—	Cd/Ga	Cd/Ga	Cd/Ga

Notes: Correlations are with a 99% confidence level. Those with 95% confidence level are given in parentheses. — = no correlation.

self contains less than 30 wt% S and consists of highly altered wall-rock with disseminated and vein-type sulfides (Constantinou, 1980).

The average Cu content of bulk samples from the interior of the TAG mound is 2.4 wt% and thus is well within the range of the Cu content of massive sulfide deposits in the Troodos ophiolite, which range from less than 0.5 to about 4.5 wt% Cu (Constantinou, 1980; Spooner, 1980). Similar to TAG, elevated Zn contents are only rarely reported for the Cyprus deposits (e.g., Agrokipia B: Constantinou and Govett, 1973; Herzig, 1988). Copper is erratically distributed in the different parts of individual orebodies in Cyprus, but generally tends to increase at the upper levels of the massive ore, which is similar to the Cu enrichment in the upper 20 m of the TAG mound. Constantinou and Govett (1973) have suggested that the enrichment of Cu in the upper zones of the Cyprus sulfide deposits is the result of a submarine enrichment process involving leaching of cupreous pyrite. This may be analogous to TAG, where the enrichment of Cu and other elements at the top of the mound is attributed to zone refining, a process in which elements that are mobilized from previously deposited sulfides in the interior of the mound by later hydrothermal fluids are transported to the surface where they reprecipitate because of mixing with ambient seawater. This leaching process ultimately results in barren pyrite mineralization without significant base metal contents as found in the TAG drill core and as described from the Troodos ophiolite (Constantinou, 1980).

Cupreous pyrite ores of the Cyprus type are generally poorly zoned in comparison to volcanogenic massive sulfide deposits in the Archean greenstone belts of Canada (e.g., Noranda, Matagami, Timmins, and Mattabi districts), the Kuroko type massive sulfide deposits in Japan, western Tasmania, Newfoundland, and the Bathurst district in New Brunswick (Large, 1977). This is also obvious from the metal distribution at the TAG mound. Here, the only metal zoning is the occurrence of a zone enriched in Cu and Zn, as well as a number of other elements such as Au, at the top of the TAG mound.

One of the most striking features of the cores recovered during Leg 158 is the abundance of anhydrite preserved within the interior of the active TAG mound, resulting in Ca concentrations of up to 11.5 wt% (Table 2). Because of its retrograde solubility, anhydrite commonly dissolves in seawater at temperatures of less than 150°C and seafloor pressures (Haymon and Kastner, 1981). The retrograde solubility of anhydrite is in part responsible for the instability and ultimate collapse of large inactive sulfide chimneys and explains why anhydrite and high Ca concentrations are absent from most ancient volcanogenic massive sulfide deposits.

A comparison of the major- and trace-element geochemistry of bulk sulfides from the interior of the TAG mound with the chemical composition of samples recovered by submersible or surface ship from the surface of seafloor hydrothermal deposits indicates important differences. The concentrations of most elements in samples from various seafloor deposits are much higher than those in samples from the interior of the TAG mound (Table 2; Herzig and Hannington, 1995). This is consistent with enrichment of surface sulfides by zone refining. Base-metal–rich chimney fragments, which are preferentially sampled by submersible or dredge, are obviously not representative for seafloor polymetallic sulfide deposits as a whole.

Sulfur-isotopic studies of seafloor massive sulfide deposits forming at the mid-ocean ridges have shown a range of $\delta^{34}S$ ratios from +0.7‰ to +6.3‰. A compilation of 501 analyses from different sediment-free mid-ocean ridge sites yields an average of +3.2‰ $\delta^{34}S$ (for references see Fig. 13). These data are explained by the fact that the sulfur originates from two different sources: mid-ocean ridge basalt (MORB, $\delta^{34}S$ = +0.1‰; Sakai et al., 1984) and seawater ($\delta^{34}S$ = +20.9‰; Rees et al., 1978). Arnold and Sheppard (1981) have calculated that the sulfur-isotopic composition of massive sulfides from the East Pacific Rise 21°N (+2.1‰ $\delta^{34}S$) can be explained by non-equilibrium mixing of about 10% reduced seawater sulfate with about 90% sulfide of basaltic origin. A $\delta^{34}S$ value of +6‰ for example would result in a seawater/basalt sulfur ratio of 30:70. Thus, the variation in sulfur-isotopic ratios of seafloor massive sulfides are explained by varying proportions of mixing between hydrothermal fluid and seawater. Anhydrite and barite associated with the precipitation of sulfides from seafloor hydrothermal fluids usually have the sulfur-isotopic composition of contemporaneous seawater.

The sulfur-isotopic ratios of +4.6‰ to +8.2‰, with an average of +6.4‰ $\delta^{34}S$ determined for bulk samples from the TAG mound are, on average, about 3‰ heavier than the average value for all other sediment-free mid-ocean ridge sulfides, but are similar to the average of stockwork pyrite from Cyprus (average +6.4‰ $\delta^{34}S$; Alt, 1994) and pyrite from massive sulfide deposits in the Troodos ophiolite (+4‰ to +7‰ $\delta^{34}S$; Alt, 1994). In some areas of the TAG mound, the $\delta^{34}S$ ratios appear to increase downhole. Sulfur-isotope studies by Knott et al. (Chap. 1, this volume) and Gemmell and Sharpe (Chap. 5, this volume) also indicate an increase of $\delta^{34}S$ ratios with depth. Furthermore, both studies reveal heavy sulfur isotope ratios (+8‰ to +10‰) for disseminated pyrite in chloritized and paragonitized basalt fragments and lighter $\delta^{34}S$ values for vein-related pyrite of the stockwork zone. Thus, the bulk sulfide $\delta^{34}S$ ratios determined in this study likely show an average of heavy sulfur in disseminated sulfides and light vein-related sulfides, obviously masking the increase of sulfur-isotopic ratios of bulk sulfides with depth.

Drilling results have indicated the presence of pyrite-anhydrite breccias at 20−45 mbsf with pyrite clasts cemented by anhydrite down to 30 mbsf. This is followed by pyrite-silica-anhydrite breccias, which are commonly crosscut by anhydrite veins up to 45 cm in thickness. The presence of anhydrite within the mound is likely explained by conductive heating of seawater close to the high-temperature feeder zone (Hannington et al., Chap. 28, this volume) and, at least to some extent, through mixing of seawater with upwelling high-temperature hydrothermal fluids (Humphris et al., 1995). At the same time, these fluids may be responsible for the thermochemical reduction of pre-existing anhydrite at temperatures well above 300°C. Part of the reduced sulfate will be carried as H_2S in the upwelling hydrothermal fluid which may explain the heavy sulfur isotopic signature found in the TAG sulfides (cf. Janecky and Shanks,

Table 6. Sulfur-isotopic composition of bulk sulfide samples from TAG-1 to TAG-5 areas at the TAG hydrothermal mound.

Area	Hole, core, section, interval (cm)	Sample type	Depth (mbsf)	Average $\delta^{34}S_{CDT}$[‰]
TAG-1				
	957C-5N-1, 15-48	Massive pyrite-anhydrite breccia	15.25	6.6
	957C-7N-1, 52-56	Nodular siliceous pyrite-anhydrite breccia	20.04	5.1
	957C-7N-2, 61-69	Nodular siliceous pyrite-anhydrite breccia	21.45	5.5
	957C-10N-1, 21-22	Massive pyrite-breccia	28.86	6.5
	957C-11N-1, 58-61	Pyrite-silica-anhydrite breccia	31.18	5.9
	957C-11N-3, 90-94	Massive pyrite breccia and anhydrite vein	34.50	5.6
	957C-12N-1, 53-59	Massive pyrite-anhydrite breccia	35.45	5.9
	957C-12N-2, 68-75	Pyrite-silica-anhydrite breccia	36.16	6.3
	957C-12N-3, 86-100	Pyrite-silica-anhydrite breccia	36.94	6.2
	957C-13N-1, 12-20	Pyrite-anhydrite breccia	37.31	5.5
	957C-14N-1, 33-41	Pyrite-silica breccia	40.53	6.0
	957C-14N-2, 76-87	Pyrite-silica breccia	41.67	6.5
	957C-15N-1, 36-40	Pyrite-silica breccia	42.50	6.4
	957C-15N-2, 12-15	Silicified wallrock breccia	43.28	7.1
	957C-15N-3, 132-150	Silicified wallrock breccia	45.54	6.4
	957C-15N-4, 8-10	Silicified wallrock breccia	45.70	7.4
	957C-16N-1, 118-125	Pyrite-anhydrite breccia	47.39	6.6
	957C-16N-2, 14-23	Silicified wallrock breccia	47.75	6.7
	957C-16N-2, 94-95	Pyrite-silica breccia	48.56	7.5
	957E-1R-1, 23-26	Nodular pyrite-silica breccia	31.70	7.9
	957E-9R-1, 16-19	Massive granular pyrite	78.16	6.3
	957E-12R-1, 16-20	Silicified wallrock breccia	91.95	6.5
	957E-15R-1, 27-30	Chloritized basalt breccia	106.77	6.7
	957F-1-N-1, 32-35	Nodular pyrite breccia	1.13	5.9
	957F-2N-1, 11-19	Massive granular pyrite	1.31	5.7
TAG-2				
	957B-1R-1, 3-95	Pyrite, iron oxides, and chert; drill cuttings	0.00	5.4
	957H-1N-1, 60-73	Porous nodular pyrite breccia	9.30	6.2
	957H-5N-1, 61-64	Nodular pyrite-silica breccia	27.30	7.3
	957H-6N-1, 14-19	Pyrite-silica breccia	31.34	7.5
TAG-3				
	957Q-1R-3, 70-100	Pyrite, iron oxide; drill cuttings	3.75	7.3
TAG-4				
	957I-1N-1, 33-40	Porous massive pyrite-marcasite	9.33	5.7
	957K-1X-1, 24-29	Porous colloform pyrite-marcasite	0.21	4.6
	957K-2N-1, 37-41	Massive granular pyrite	10.37	5.7
	957K-3X-1, 36-38	Massive pyrite with silica	14.82	6.0
	957M-2R-1, 2-5	Porous massive pyrite	9.30	7.4
	957M-3R-1, 57-60	Massive granular pyrite	14.87	6.3
	957M-3R-1, 123-125	Pyrite-silica breccia with late marcasite	15.49	6.4
	957M-3R-2, 1-4	Pyrite-silica breccia	15.80	7.2
	957M-5R-1, 89-91	Pyrite-silica breccia	25.18	8.2
	957M-8R-1, 0-4	Massive granular pyrite	38.30	6.0
TAG-5				
	957O-2R-1, 22-24	Nodular pyrite breccia	8.10	5.6
	957O-4R-1, 45-50	Pyrite-anhydrite breccia	16.35	5.9
	957P-1R-1, 44-46	Pyrite-anhydrite breccia	0.43	6.1
	957P-5R-1, 9-13	Pyrite-anhydrite breccia	21.57	5.7
	957P-10R-1, 1-3	Massive pyrite	45.10	5.4
	957P-12R-1, 15-100	Drill cuttings; pyrite-anhydrite sand	54.40	6.5
	957P-12R-2, 25-28	Pyrite-silica breccia	55.89	8.1
	957P-12R-4, 53-57	Massive porous pyrite with pyrite-silica clasts	57.61	6.3
	957P-13W-1, 50-58	Pyrite-anhydrite sand; drill cuttings	15.00	6.5

Table 7. Sulfur-isotopic composition of bulk sulfide samples from TAG-1 to TAG-5 areas and different lithologic zones, with averages for all samples analyzed from the TAG mound.

Area or lithologic zone	n	Range	Average
TAG-1	25	5.10-7.90	6.4
TAG-2	4	5.35-7.47	6.6
TAG-3	1	7.30	7.3
TAG-4	10	4.60-8.15	6.3
TAG-5	9	5.40-8.13	6.2
TAG	49	4.60-8.15	6.4
Massive pyrite + pyrite breccias	11	4.60-7.10	5.8
Pyrite-anhydrite ± silica breccias	14	5.10-6.60	5.9
Pyrite-silica breccias	14	5.40-8.15	6.8
Silicified wallrock breccias	8	6.25-7.50	6.8
Chloritized basalt breccias	1	6.70	6.7

Note: n = number of samples.

1988; Shanks et al., 1995). Simple mixing of end-member hydrothermal fluids with a $\delta^{34}S$ ratio close to the initial basalt values (+0.1‰, Sakai et al., 1984) with seawater cannot account for the elevated $\delta^{34}S$ values of the TAG sulfides. High $\delta^{34}S$ ratios for bulk sulfides have also been found for massive sulfides from the relict *Mir* and *Alvin* zones with in the TAG hydrothermal field, ranging from +2.2‰ to +7.3‰ $\delta^{34}S$ (average +5.9‰, n = 6). This suggests that elevated sulfur-isotope ratios are not limited to the active TAG mound, but are a common phenomenon in the TAG hydrothermal system.

ACKNOWLEDGMENTS

This work was supported through a grant of the Deutsche Forschungsgemeinschaft (DFG grant No. He 1660/5) and NATO Scientific Affairs Division (CRG grant No. 941218). Thanks are due to M. Tichomirowa and R. Liebscher for help with sulfur isotope analyses. Comments by R. Zierenberg and B. Taylor greatly improved the manuscript.

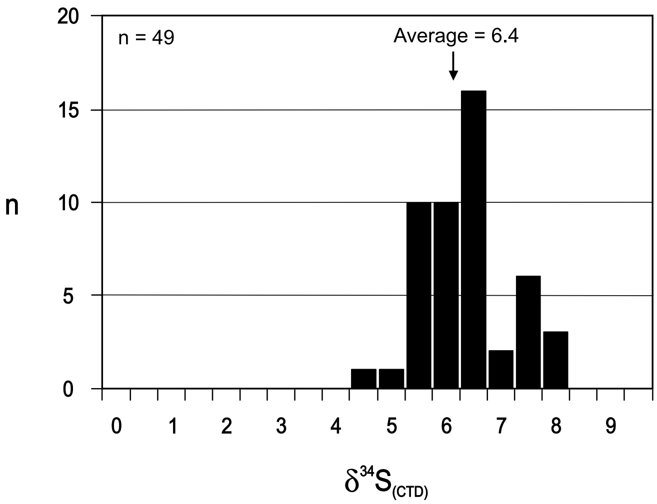

Figure 11. Frequency distribution of sulfur-isotopic ratios for 49 bulk sulfide samples analyzed from the interior of the TAG hydrothermal mound (‰ $\delta^{34}S$). n = number of samples.

REFERENCES

Alt, J.C., 1994. A sulfur isotopic profile through the Troodos ophiolite, Cyprus: primary composition and the effects of seawater hydrothermal alteration. *Geochim. Cosmochim. Acta*, 58:1825–1840.

Arnold, M., and Sheppard, S.M.F., 1981. East Pacific Rise at latitude 21°N: isotopic composition and origin of the hydrothermal sulfur. *Earth Planet. Sci. Lett.* 56:148–156.

Blum, N., and Puchelt, H., 1991. Sedimentary-hosted polymetallic massive sulfide deposits of the Kebrit and Shaban Deeps, Red Sea. *Miner. Deposita*, 26:217–227.

Bluth, G.J., and Ohmoto, H., 1988. Sulfide-sulfate chimneys on the East Pacific Rise, 11° and 13°N latitude. Part II: sulfur isotopes. *Can. Mineral.*, 26:505–515.

Böhlke, J.K., and Shanks, W.C., III., 1994. Stable isotope study of hydrothermal vents at Escanaba Trough: observed and calculated effects of sediment-seawater interaction. *In* Morton, J.L., Zierenberg, R.A., and Reiss, C.A. (Eds.), *Geologic, Hydrothermal and Biologic Studies at Escanaba Trough, Gorda Ridge, Offshore Northern California.* U.S. Geol. Surv. Bull., 2022:223–239.

Constantinou, G., 1980. Metallogenesis associated with the Troodos ophiolite. *In* Panayioutou, A. (Ed.), *Ophiolites.* Proc. Int. Ophiolite Symp. Cyprus, Cyprus Geol. Surv. Dep., 663–674.

Constantinou, G., and Govett, G.J.S., 1973. Geology, geochemistry, and genesis of Cyprus sulfide deposits. *Econ. Geol.*, 68:843–858.

Crocket, J.H., 1991. Distribution of gold in the Earth's crust. *In* Foster, R.P. (Ed.), *Gold Metallogeny and Exploration:* Glasgow (Blackie and Son), 1–36.

Duckworth, R.C., Fallick, A.E., and Rickard, D., 1994. Mineralogy and sulfur isotopic composition of the Middle Valley massive sulfide deposit, northern Juan de Fuca Ridge. *In* Mottl, M.J., Davis, E.E., Fisher, A.T., and Slack, J.F. (Eds.), *Proc. ODP, Sci. Results,* 139: College Station, TX (Ocean Drilling Program), 373–385.

Duckworth, R.C., Knott, R., Fallick, A.E., Rickard, D., Murton, B.J., and Van Dover, C., 1995. Mineralogy and sulfur isotope geochemistry of the Broken Spur sulfides, 29°N, Mid-Atlantic Ridge. *In* Parson, L.M., Walker, C.L., and Dixon, D.R. (Eds.), *Hydrothermal Vents and Processes.* Geol. Soc. Spec. Publ. London, 87:175–189.

Edmond, J.M., Campbell, A.C., Palmer, M.R., German, C.R., Klinkhammer, G.P., Edmonds, H.N., Elderfield, H., Thompson, G., and Rona, P., 1995. Time series studies of vent fluids from the TAG and MARK sites (1986, 1990): Mid-Atlantic Ridge: a new solution chemistry model and a mechanism for Cu/Zn zonation in massive sulfide ore bodies. *In* Parson, L.M., Walker, C.L., and Dixon, D.R. (Eds.), *Hydrothermal Vents and Processes.* Geol. Soc. Spec. Publ. London, 87:77–86.

Goodfellow, W.D., and Blaise, B., 1988. Sulfide formation and hydrothermal alteration of hemipelagic sediment in Middle Valley, northern Juan de Fuca Ridge. *Can. Mineral.*, 26:675–696.

Halbach, P., Nakamura, K., Washner, M., Lange, J., Sakai, H., Kaselitz, L., Hansen, R.D., Yamano, M., Post, J., Prause, B., Seifert, R., Michaelis, W., Teichmann, F., Kinoshita, M., Marten, A., Ishibashi, J., Czerwinski, S., and Blum, N., 1989. Probable modern analogue of Kuroko-type massive sulfide deposits in the Okinawa Trough back-arc basin. *Nature*, 338:496–499.

Hannington, M.D., Herzig, P.M., and Scott, S.D., 1991. Auriferous hydrothermal precipitates on the modern seafloor. *In* Foster, R.P. (Ed.), *Gold Metallogeny and Exploration:* Glasgow (Blackie and Son), 249–282.

Hannington, M.D., and Scott, S.D., 1988. Mineralogy and geochemistry of an hydrothermal silica-sulfide-sulfate spire in the caldera of Axial-Seamount, Juan de Fuca Ridge. *Can. Mineral.*, 26:603–625.

Haymon, R.M., and Kastner, M., 1981. Hot spring deposits on the East Pacific Rise at 21°N: preliminary description of mineralogy and genesis. *Earth Planet. Sci. Lett.*, 53:363–381.

Hekinian, R., Fevrier, M., Bischoff, J.L., Picot, P., and Shanks, W.C., 1980. Sulfide deposits from the East Pacific Rise near 21°N. *Science*, 207:1433–1444.

Herzig, P.M., 1988. A mineralogical, geochemical, and thermal profile through the Agrokipia "B" hydrothermal sulfide deposit, Troodos ophiolite complex, Cyprus. *In* Friedrich, G.H., and Herzig, P.M. (Eds.), *Base Metal Sulfide Deposits in Sedimentary and Volcanic Environments:* Berlin (Springer-Verlag), 182–215.

Herzig, P.M., and Hannington, M.D., 1995. Polymetallic massive sulfides at the modern seafloor—a review. *Ore Geol. Rev.*, 10:95–115.

Herzig, P.M., Hannington, M.D., and Arribas, A., Jr., in press. Sulfur isotopic composition of hydrothermal precipitates from the Lau back-arc: implications for magmatic contributions to seafloor hydrothermal systems. *Mineral. Deposita.*

Herzig, P.M., Hannington, M.D., Scott, S.D., Maliotis, G., Rona, P.A., and Thompson, G., 1991. Gold-rich seafloor gossans in the Troodos ophiolite and on the Mid-Atlantic Ridge. *Econ. Geol.*, 86:1747–1755.

Humphris, S.E., Herzig, P.M., Miller, D.J., Alt, J.C., Becker, K., Brown, D., Brügmann, G., Chiba, H., Fouquet, Y., Gemmell, J.B., Guerin, G., Hannington, M.D., Holm, N.G., Honnorez, J.J., Itturino, G.J., Knott, R., Ludwig, R., Nakamura, K., Petersen, S., Reysenbach, A.-L., Rona, P.A., Smith, S., Sturz, A.A., Tivey, M.K., and Zhao, X., 1995. The internal structure of an active sea-floor massive sulphide deposit. *Nature*, 377:713–716.

Janecky, D.R., and Shanks, W.C., III, 1988. Computational modeling of chemical and sulfur isotopic reaction processes in seafloor hydrothermal systems: chimneys, massive sulfides, and subjacent alteration zones. *Can. Mineral.*, 26:805–825.

Kase, K., Yamamoto, M., and Shibata, T., 1990. Copper-rich sulfide deposit near 23°N, Mid-Atlantic Ridge: chemical composition, mineral chemistry, and sulfur isotopes. *In* Detrick, R., Honnorez, J., Bryan, W.B., Juteau, T., et al., *Proc. ODP, Sci. Results,* 106/109: College Station, TX (Ocean Drilling Program), 163–177.

Kerridge, J., Haymon, R.M., and Kastner, M., 1983. Sulfur isotope systematics at the 21°N site, East Pacific Rise. *Earth Planet. Sci. Lett.*, 66:91–100.

Kleinrock, M.C., Humphris, S.E., and the Deep-TAG Team, 1996. Detailed structure and morphology of the TAG active hydrothermal mound and its geotectonic environment. *In* Humphris, S.E., Herzig, P.M., Miller, D.J., et al., *Proc. ODP, Init. Repts.*, 158: College Station, TX (Ocean Drilling Program), 15–21.

Knott, R., Fallick, A.E., Rickard, D., and Bäcker, H., 1995. Mineralogy and sulphur isotope characteristics of a massive sulphide boulder, Galapagos Rift, 85°55′W. *In* Parson, L.M., Walker, C.L., and Dixon, D.R. (Eds.), *Hydrothermal Vents and Processes.* Geol. Soc. Spec. Publ. London, 87:207–222.

Koski, R.A., Shanks, W.C., III, Bohrson, W.A., and Oscarson, R.L., 1988. The composition of massive sulfide deposits from the sediment-covered floor of Escanaba Trough, Gorda Ridge: implications for depositional processes. *Can. Mineral.*, 26:655–673.

Kusakabe, M., Mayeda, S., and Nakamura, E., 1990. S, O and Sr isotope systematics of active vent materials from the Mariana backarc basin spreading axis at 18°N. *Earth Planet. Sci. Lett.*, 100:275–282.

Lalou, C., Reyss, J.L., Brichet, E., Arnold, M., Thompson, G., Fouquet, Y., and Rona, P.A., 1993. New age data for Mid-Atlantic Ridge hydrothermal sites: TAG and Snakepit geochronology revisited. *J. Geophys. Res.*, 98:9705–9713.

Large, R.R., 1977. Chemical evolution and zonation of massive sulfide deposits in volcanic terrains. *Econ. Geol.*, 72:549–572.

Lein, A.Y., Ul'yanova, N.V., Grinenko, V.A., Bibikova, Ye.V., and Lisitsyn, A.P., 1993. Mineralogical and geochemical features of the Manus Basin hydrothermal sulfide ores, Bismarck Sea. *Geochem. Int.*, 30:57–71.

Lein, A.Y., Ul'yanova, N.V., Grinenko, V.A., and Lisitsyn, A.P., 1991. Geochemistry of the hydrothermal sulfide ores of the Mid-Atlantic Ridge (26°N). *Geochem. Int.*, 28:1–13.

Marchig, V., Puchelt, H., Rosch, H., and Blum, N., 1990. Massive sulfides from ultra-fast spreading ridge, East Pacific Rise at 18–21°S: a geochemical stock report. *Mar. Min.*, 9:459–493.

McConachy, T.F., 1988. Hydrothermal plumes and related deposits over spreading ridges in the northeast Pacific Ocean: the East Pacific Rise near 11°N and 21°N, Explorer Ridge, and the J. Tuzo Wilson Seamounts [Ph.D. thesis]. Univ. of Toronto.

Peter, J.M., and Shanks, W.C., III, 1992. Sulfur, carbon, and oxygen isotope variations in submarine hydrothermal deposits of Guaymas Basin, Gulf of California, U.S.A. *Geochim. Cosmochim. Acta,* 56:2025–2040.

Rees, C.E., Jenkins, W.J., and Monster, J., 1978. The sulphur isotopic composition of ocean water sulphate. *Geochim. Cosmochim. Acta,* 42:377–381.

Rona, P.A., Hannington, M.D., Raman, C.V., Thompson, G., Tivey, M.K., Humphris, S.E., Lalou, C., and Petersen, S., 1993. Active and relict seafloor hydrothermal mineralization at the TAG hydrothermal field, Mid-Atlantic Ridge. *Econ. Geol.*, 88:1987–2013.

Rona, P.A., Klinkhammer, G., Nelson, T.A., Trefry, J.H., and Elderfield, H., 1986. Black smokers, massive sulfides and vent biota on the Mid-Atlantic Ridge. *Nature*, 321:33–37.

Rona, P.A., Petersen, S., Becker, K., Von Herzen, R.P., Hannington, M.D., Herzig, P.M., Naka, J., Lalou, C., and Thompson, G., 1996. Heat flow and mineralogy of TAG relict high-temperature hydrothermal zones; Mid-Atlantic Ridge 26°N, 45°W. *Geophys. Res. Lett.*, 23:3507–3510.

Rona, P.A., Thompson, G., Mottl, M.J., Karson, J.A., Jenkins, W.J., Graham, D., Mallette, M., Von Damm, K., and Edmond, J.M., 1984. Hydrothermal activity at the TAG hydrothermal field, Mid-Atlantic Ridge crest at 26°N. *J. Geophys. Res.*, 89:11365–11377.

Sakai, H., Des Marais, D.J., Ueda, A., and Moore, J.G., 1984. Concentrations and isotope ratios of carbon, nitrogen and sulfur in ocean-floor basalts. *Geochim. Cosmochim. Acta,* 48:2433–2441.

Shanks, W.C., III., Böhlke, J.K., Seal, R.R., II, 1995. Stable isotopes in mid-ocean ridge hydrothermal systems: interactions between fluids, minerals, and organisms. *In* Humphris, S.E., Zierenberg, R.A., Mullineaux, L.S., Thompson, R.E. (Eds.), *Seafloor Hydrothermal Systems: Physical, Chemical, Biological, and Geological Interactions.* Geophys. Monogr., 91:194–221.

Shanks, W.C., III, and Seyfried, W.E., Jr., 1987. Stable isotope studies of vent fluids and chimney minerals, southern Juan de Fuca Ridge: sodium metasomatism and seawater sulfate reduction. *J. Geophys. Res.*, 92:11387–11399.

Skirrow, R., and Coleman, M.L., 1982. Origin of sulfur and geothermometry of hydrothermal sulfides from the Galapagos Rift, 86°N. *Nature*, 299:142–144.

Spooner, E.T.C., 1980. Cu-pyrite mineralization and seawater convection in oceanic crust. *Geol. Assoc. Can., Spec. Pap.,* 20:685–704.

Stuart, F.M., Harrop, P.J., Knott, R., Fallick, A.E., Turner, G., Fouquet, Y., and Rickard, D., 1995. Noble gas isotopes in 25,000 years of hydrothermal fluids from 13°N on the East Pacific Rise. *In* Parson, L.M., Walker, C.L., and Dixon, D.R. (Eds.), *Hydrothermal Vents and Processes.* Geol. Soc. Spec. Publ. London, 87:133–143.

Stuart, F.M., Turner, G., Duckworth, R.C., and Fallick, A.E., 1994. Helium isotopes as tracers of trapped hydrothermal fluids in ocean-floor sulfides. *Geology*, 22:823–826.

Styrt, M.M., Brackmann, A.J., Holland, H.D., Clark, B.C., Pisutha-Arnond, V., Eldridge, C.S., and Ohmoto, H., 1981. The mineralogy and isotopic composition of sulfur in hydrothermal sulfide/sulfate deposits on the East Pacific Rise, 21°N latitude. *Earth Planet. Sci. Lett.*, 53:382–390.

Thompson, G., Humphris, S.E., Schroeder, B., Sulanowska, M., and Rona, P.A., 1988. Active vents and massive sulfides at 26°N (TAG) and 23°N (Snakepit) on the Mid-Atlantic Ridge. *Can. Mineral.*, 26:697–711.

Tivey, M.K., Humphris, S.E., Thompson, G., Hannington, M.D., and Rona, P.A., 1995. Deducing patterns of fluid flow and mixing within the TAG active hydrothermal mound using mineralogical and geochemical data. *J. Geophys. Res.*, 100:12527–12555.

Ueda, A., and Krouse, H.R., 1986. Direct conversion of sulfide and sulfate minerals to SO_2 for isotope analyses. *Geochem. J.*, 20:209–212.

Woodruff, L.G., and Shanks, W.C., 1988. Sulfur isotope study of chimney minerals and hydrothermal fluids from 21°N, East Pacific Rise: hydrothermal sulfur sources and disequilibrium sulfate reduction. *J. Geophys. Res.*, 93:4562–4572.

Zierenberg, R.A., 1994. *Data Report:* Sulfur content of sediment and sulfur isotope values of sulfide and sulfate minerals from Middle Valley. *In* Mottl, M.J., Davis, E.E., Fisher, A.T., and Slack, J.F. (Eds.), *Proc. ODP, Sci. Results*, 139: College Station, TX (Ocean Drilling Program), 739–748.

Zierenberg, R.A., Koski, R.A., Morton, J.L., Bouse, R.M., and Shanks, W.C., III, 1993. Genesis of massive sulfide deposits on a sediment-covered spreading center, Escanaba Trough, 41°N, Gorda Ridge. *Econ. Geol.*, 88:2069–2098.

Zierenberg, R.A., Shanks, W.C., III., and Bischoff, J.L., 1984. Massive sulfide deposits at 21°, East Pacific Rise: chemical composition, stable isotopes, and phase equilibria. *Geol. Soc. Am. Bull.*, 95:922–929.

Date of initial receipt: 5 June 1996
Date of acceptance: 31 March 1997
Ms 158SR-202

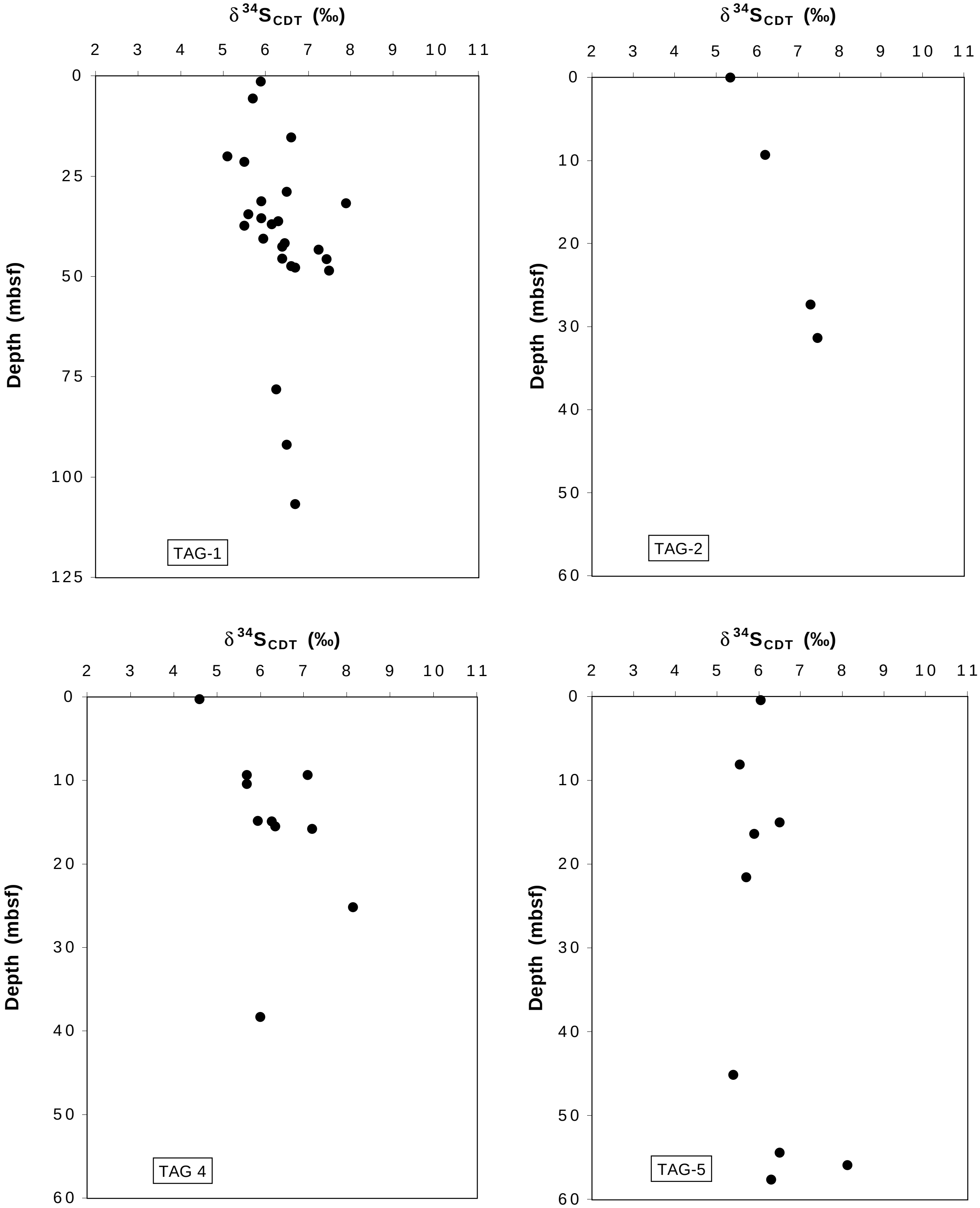

Figure 12. Downhole distribution of $\delta^{34}S$ ratios in bulk sulfide samples from the TAG-1, -2, -4, and -5 areas.

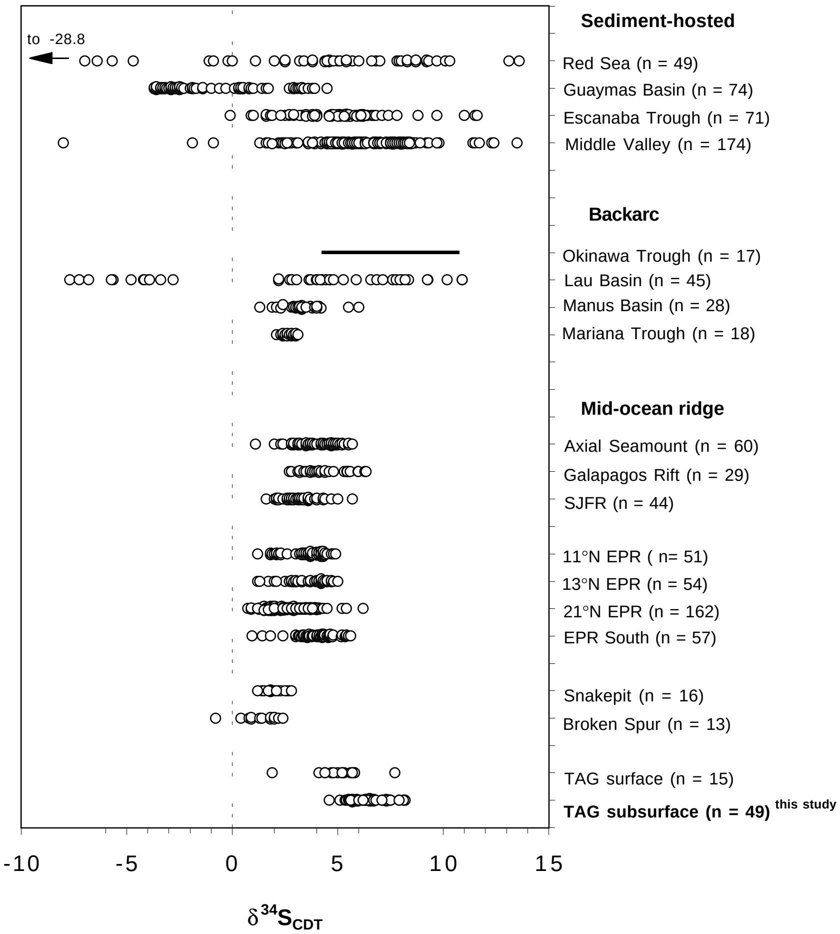

Figure 13. Sulfur-isotopic ratios in various types of seafloor massive sulfide deposits, including sediment-hosted mid-ocean ridge sulfides, backarc sulfides, and sediment-free mid-ocean ridge sulfides. The sulfur-isotopic ratios determined for drill core sulfides from the TAG hydrothermal field are shown for comparison (‰ $\delta^{34}S$). References: Red Sea = Blum and Puchelt (1991); Guaymas Basin = Peter and Shanks (1992); Escanaba Trough = Koski et al. (1988), Zierenberg et al. (1993), Böhlke and Shanks (1994); Middle Valley = Goodfellow and Blaise (1988), Duckworth et al. (1994), Zierenberg (1994); Stuart et al., (1994); Okinawa Trough = Halbach et al. (1989); Lau Basin = Herzig et al. (in press); Manus Basin = Lein et al. (1993); Mariana Trough = Kusakabe et al. (1990); Axial Seamount = Hannington and Scott (1988); Galapagos Rift = Skirrow and Coleman (1982); Knott et al. (1995); Southern Juan de Fuca Ridge (SJFR) = Shanks and Seyfried (1987); 11°N East Pacific Rise (EPR) = McConachy (1988); Bluth and Ohmoto (1988); 13°N EPR = Bluth and Ohmoto (1988), Stuart et al. (1995); 21°N EPR = Hekinian et al. (1980), Arnold and Sheppard (1981), Styrt et al. (1981), Kerridge et al. (1983), Zierenberg et al. (1984), Woodruff and Shanks (1988); Stuart et al., (1994); EPR South = Marchig et al. (1990); Snakepit = Kase et al. (1990); Stuart et al., (1994); Broken Spur = Duckworth et al. (1995); TAG surface = Stuart et al. (1994); Lein et al., 1991; TAG subsurface = this study.